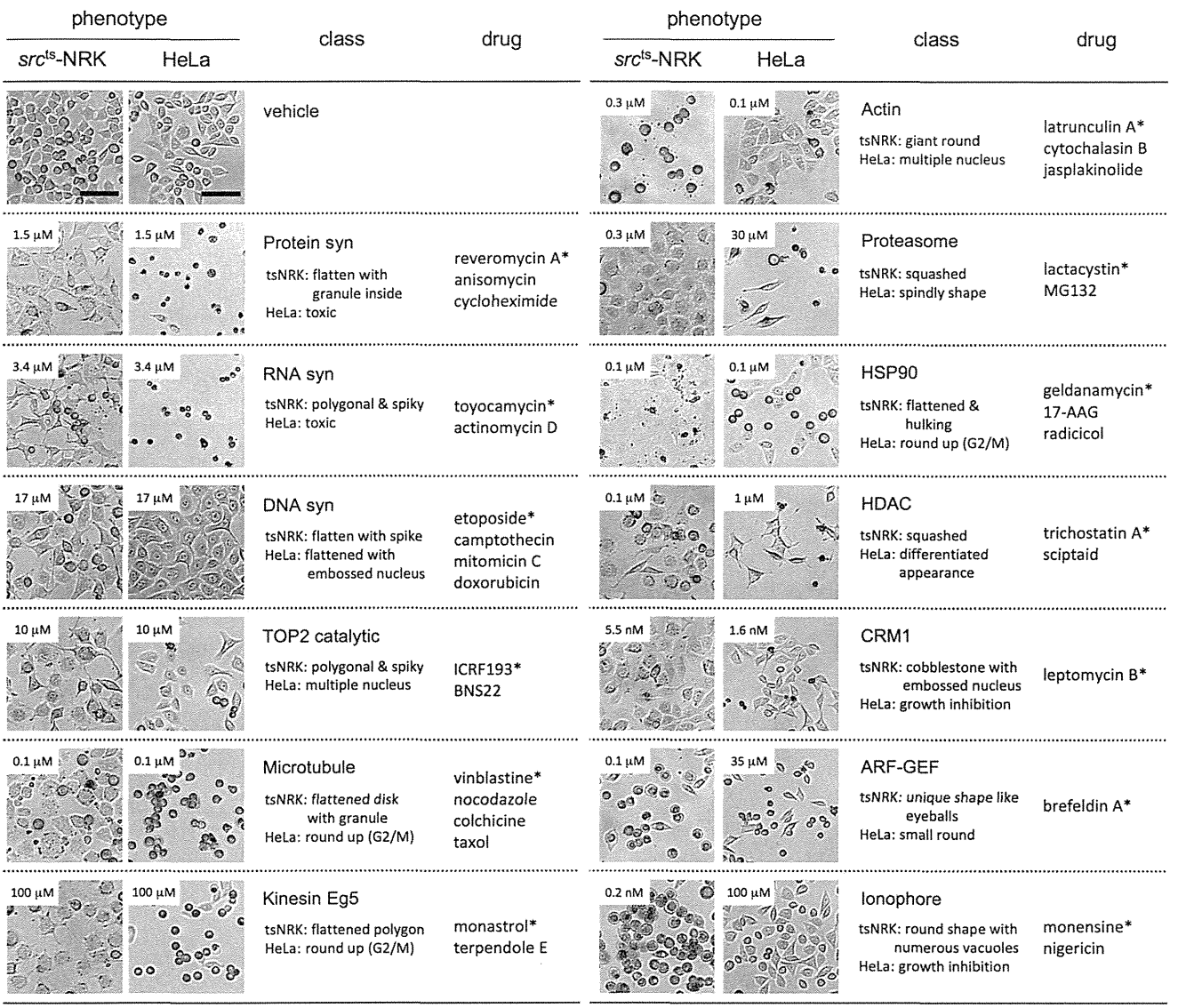

Figure 1. A Variety of Cell Shape Changes in *src*^{ts}-NRK Cells Induced by Well-Characterized Drugs Classified by Mode of Action

src^{ts}-NRK and HeLa cells were treated with well-characterized drugs at various concentrations and times. Representative images are shown of morphological changes of *src*^{ts}-NRK cells and HeLa cells observed under a microscope at 48 and 24 hr after treatment of a drug marked by an asterisk (*). Scale bars, 100 μm. See also Figure S1.

Hoechst 33342 to visualize the nuclei. Using IN Cell Analyzer, images of up to 1,500 cells from each well were collected and analyzed using the image segmentation procedures above. A set of descriptors, such as "Nuclear," "Cell," and "Granule," was applied to each cell. To characterize "well-level" responses, each parametric measurement was averaged, and the median and SD were calculated to account for bi- or polyphasic phenotype responses, such as a mixture of large and small cells (Figure 3). In total, 71 parameters were identified from 24 descriptors, yielding 14,697 data points (71 parameters × 207 compounds).

To analyze this amount of multiparametric data, we developed a data analysis program that incorporates multivariate statistical tools to automatically analyze, visualize, and rank multiparametric high-content phenotype results. Principal component analysis (PCA) was applied to visualize the multiparametric phenotype responses, and morphological similarities were defined using our original index, termed "probability scores" and Euclidean distance (Figure 3). Figure 4 shows the projection of the samples' PCA scores onto the first two principal components, which explains approximately 50% of variation in the data set. The black dots in the middle represent the group of vehicle controls; other spots on the 2D scatterplots represent individual compounds, and the points of well-characterized drugs are colored by target based on the literature. As a result, drugs that had similar activities formed a cluster: the drugs with a similar effect were circled by the same dotted lines, wherein specific phenotypic responses were shown as distinct

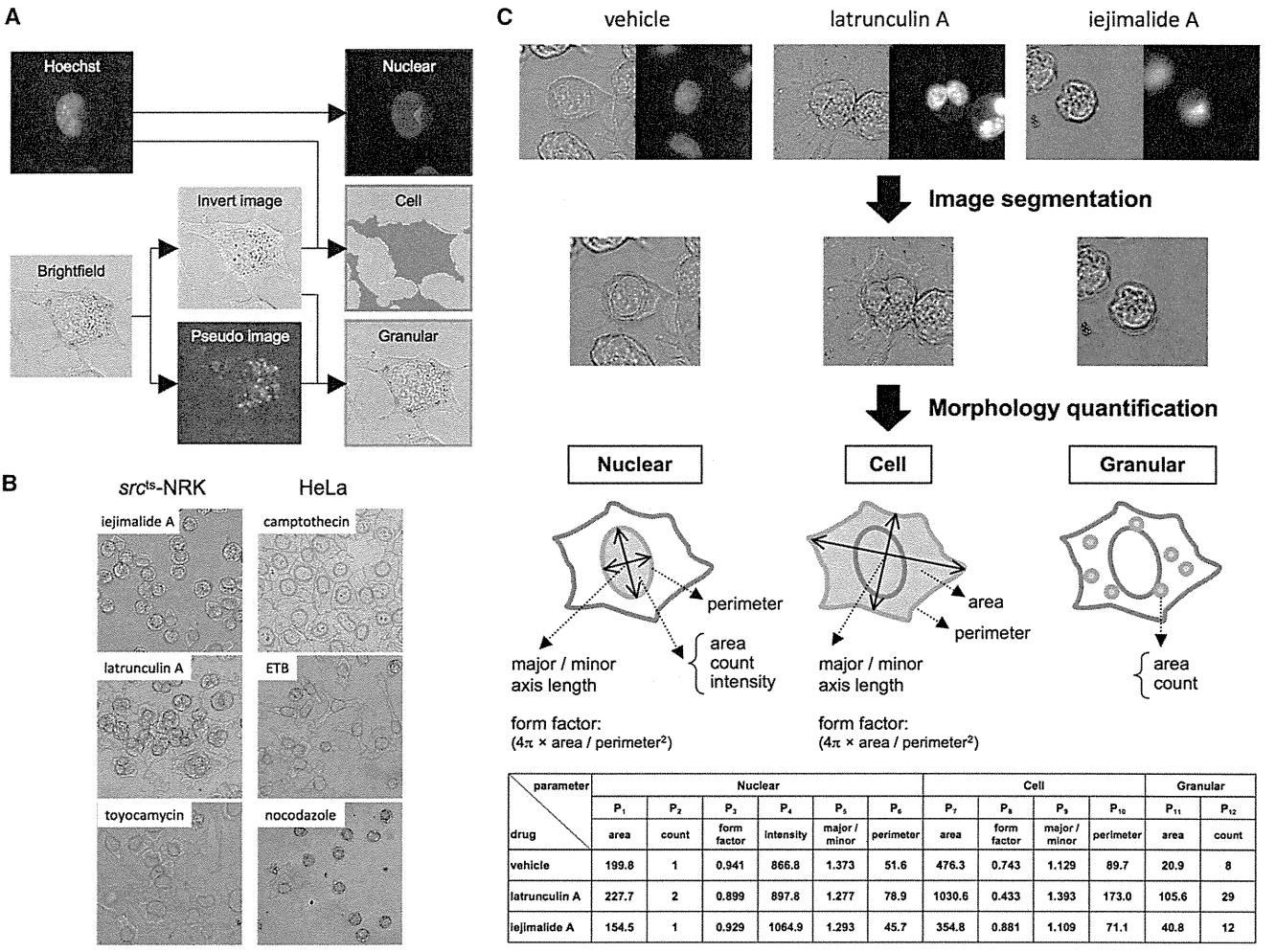

parameter / drug	Nuclear						Cell				Granular	
	P_1	P_2	P_3	P_4	P_5	P_6	P_7	P_8	P_9	P_{10}	P_{11}	P_{12}
	area	count	form factor	intensity	major / minor	perimeter	area	form factor	major / minor	perimeter	area	count
vehicle	199.8	1	0.941	866.8	1.373	51.6	476.3	0.743	1.129	89.7	20.9	8
latrunculin A	227.7	2	0.899	897.8	1.277	78.9	1030.6	0.433	1.393	173.0	105.6	29
iejimalide A	154.5	1	0.929	1064.9	1.293	45.7	354.8	0.881	1.109	71.1	40.8	12

Figure 2. Flowchart of Image Processing and Quantification of Morphological Parameters

(A) Scheme of the image segmentation program. The input images of bright-field and the same Hoechst 33342-stained cells were used for "Nuclear," "Cell," and "Granular" segmentation. "Nuclear" (blue) was assigned a nuclear-stained image. "Cell" (red) segmentation was achieved by allocating "Cell center," derived from the inverted bright-field image and nuclear information. "Granular" (pink) was defined based on inverted and pseudofluorescence bright-field images.

(B) Representative examples of the broad spectrum of heterogenic phenotype captures induced by distinct compounds. Nuclear and Cell region are colored in blue and red, respectively. The pink bullets show Granular structures, and the yellow lines show Cell center.

(C) Scheme of image processing and morphology parameter measurement. After *src*^{ts}-NRK or HeLa cells were segmented, 12 morphological parameters (P1–P12) were quantified for each cell.

See also Table S1.

distributions in the scatterplots. For instance, when we ranked the nearest neighbors to every tubulin-targeted compound by similarity, as determined by Euclidean distance metrics, typical microtubule inhibitors nearly always ranked in the top 20 (Figure 4; Table S2). Similarly, other inhibitors with typical modes of action, such as macromolecular synthesis, HDAC, and HSP, were also well classified (Table S2), suggesting that our high-content system can be successful in profiling phenotypes by drug function and in a copy mimicking the visual observation.

In this system, given that test compounds form a cluster with certain reference drugs of the data set, they are likely to have similar or identical cellular targets. We chose a well-characterized drug set, comprising 54 drugs with 14 molecular targets (Table S1), to encompass common mechanisms of toxicity and therapeutic actions against cancer cells. Then, we developed a training algorithm that determines which of the 14 target class in the training set were plausible candidates for compounds of interest by "probability scores," the mean Z scores for a test compound to the median point of each target class (see Experimental Procedures).

We employed three bioactive compounds (rotenone, 3-ATA, resveratrol) to evaluate our proposed method. Rotenone is a specific inhibitor of mitochondrial complex I, and 3-ATA was developed as a CDK4 kinase inhibitor in vitro (Kubo et al., 1999). Resveratrol has multiple activities, such as antioxidant, anti-inflammatory, and anticancer properties (Frémont, 2000). These compounds were tested in a newly established cell morphology system and primarily expressed two characteristics (Figure 5A). The high-content image profiling suggested that rotenone was significantly associated with the tubulin cluster

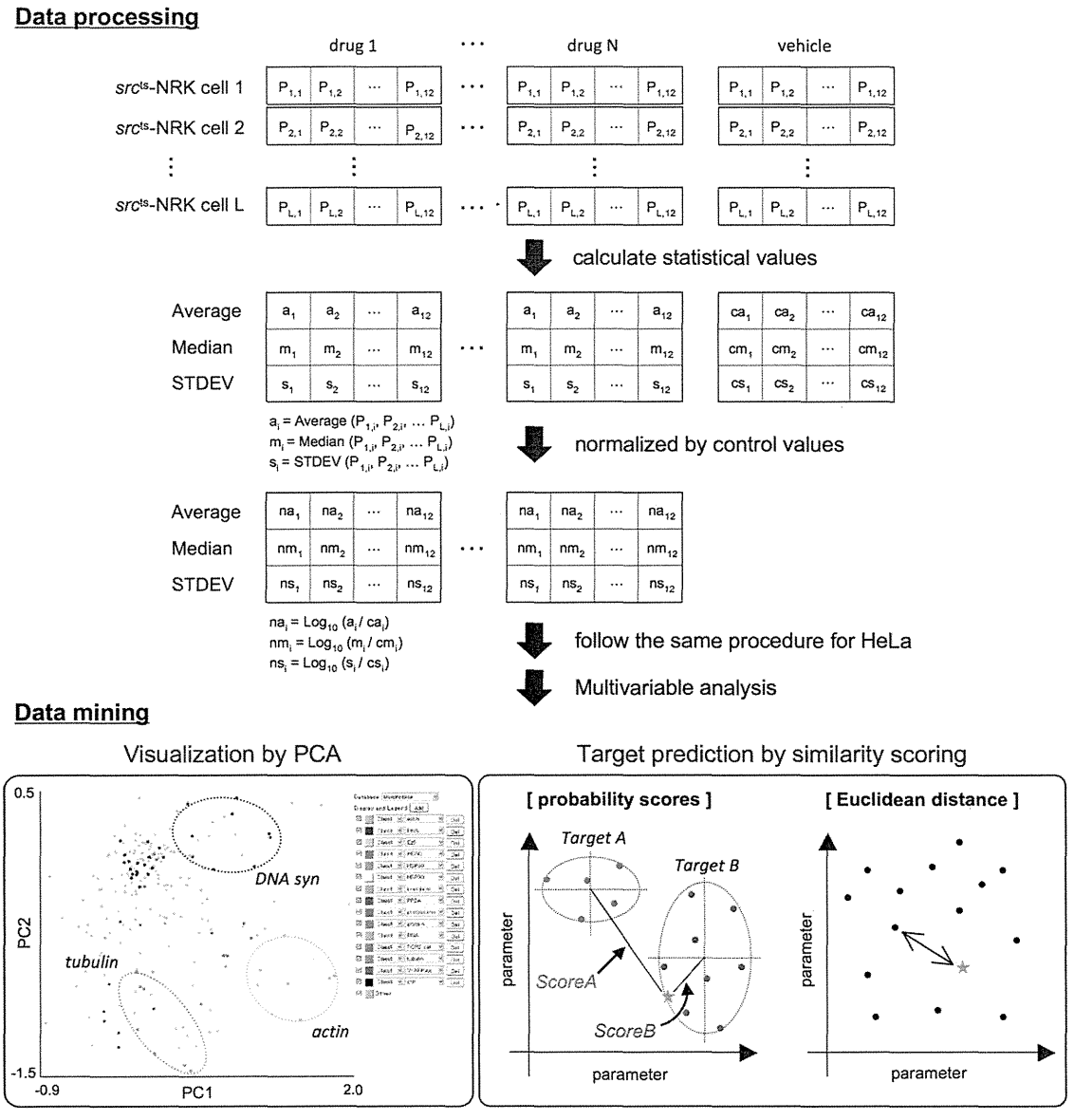

Figure 3. Schematic of Data Processing and Data Mining Step

Statistical values (Average, Median, SD) of obtained morphological parameters for ~1,000 drug N-treated *src*^{ts}-NRK and HeLa cells were calculated and normalized to the control average values as drug N-specific phenotypic multiparameters. Phenotypic multiparameters of 207 test compounds profiled by multivariate statistical analysis are illustrated. Morphobase profiling results are visualized by PCA, and the similarities in morphological changes between a compound of interest and reference compounds are defined using two statistical computations. See also Table S1.

($Score_{tubulin}$ = 1.03) and that 3-ATA and resveratrol were associated with the inhibitors of DNA synthesis ($Score_{DNA}$ = 1.56 and 0.92, respectively), based on probability scores (Figure 5B) and the rank of the top 20 nearest neighbors (Table S3). Actually, these compounds also induce other effects that are unrelated to the primary targets. Rotenone is an effective mitotic agent (Brinkley et al., 1974), 3-ATA affects DNA synthesis in an intact cell system (Diccianni et al., 2004), and most recent literature described that resveratrol acts as a TOP2 poison in cancer cells (Leone et al., 2010). Morphobase mostly provided the responsible target for the growth inhibition and deduced their reported side effects in the aforementioned case, indicating that our profiling approach detects the targets of drug candidates and determines their mechanisms of action.

Target Prediction of Compounds of Interest by Morphobase Profiling

Through our phenotypic screening of a chemical library in NPDepo, we identified several hundreds of compounds that inhibited the growth of the human promyelocytic leukemia cell line HL-60. In particular, NPD6689, NPD8617, and NPD8969 were very potent, as evidenced by the nanomolar ranges of their IC_{50} values (Table 1). By cell-cycle analysis of HeLa cells that were exposed to NPD6689 for 24 hr, the population in G2/M

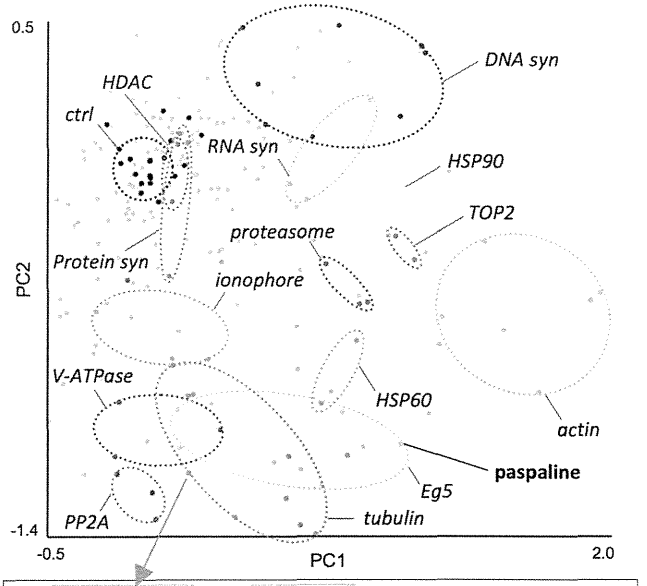

Sample podophyllotoxin Database Morphobase

Class			Sample				
Rank	Class	Score	Rank	Sample	Class	Target	MOA	Distance
1	tubulin	0.71	1	podophyllotoxin	tubulin	tubulin	microtubule dynamics	0.00
2	ionophore	2.31	2	colchicine	tubulin	tubulin	microtubule dynamics	0.63
3	PP2A	2.54	3	nocodazole	tubulin	tubulin	microtubule dynamics	0.83
4	Eg5	2.74	4	SB225002		CXCR2	chemokine receptor	0.84
5	DNA	2.94	5	benomyl	tubulin	tubulin	microtubule dynamics	0.85
6	V-ATPase	3.09	6	vinblastine	tubulin	tubulin	microtubule dynamics	0.89
7	actin	3.88	7	monensin	ionophore	Na+	vesicle trafficking	0.90
8	HSP60	3.94	8	Aurora inhibitor III		Aurora A	mitotic kinase	0.92
9	RNA	4.17	9	NPD8617		tubulin	microtubule dynamics	0.94
10	HSP90	4.44	10	cantharidin	PP2A	PP1/PP2A	phosphatase	0.95
11	proteasome	5.55	11	NPD6689		tubulin	microtubule dynamics	0.97
12	HDAC	5.91	12	okadaic acid	PP2A	PP1/PP2A	phosphatase	0.97
13	ctrl	6.00	13	concanamycin A	V-ATPase	V-ATPase	vesicle trafficking	0.97
14	protein	7.85	14	rotenone		complex I, tubulin	mitochondria respiration	0.98
15	TOP2 cat	11.29	15	toutomycin	PP2A	PP1/PP2A	phosphatase	0.99
			16	indirubin-3'-monoxime		GSK3b	GSK3b	1.00
			17	PDGFR inhibitor IV		PDGFR	RTK	1.02
			18	paclitaxel	tubulin	tubulin	microtubule dynamics	1.02
			19	ATM/ATR kinase inhibitor		ATM	ATM	1.02
			20	zGLFGMK		cathepsin G	peptidase	1.04

Figure 4. Overview of Morphobase Profiling

The user interface displays the results of principle component scores in a 2D scatterplot. The well-defined clusters can be distinguished from others by their mechanisms of action. It also displays the compound's predicted mode of action and its probability score: smaller scores reflect higher probabilities. It next ranks the 20 nearest neighbors of a test compound based on the Euclidean distance between the selected compound's positions. ctrl, control; syn, synthesis. See also Figures S5 and S6 and Tables S1 and S2.

A

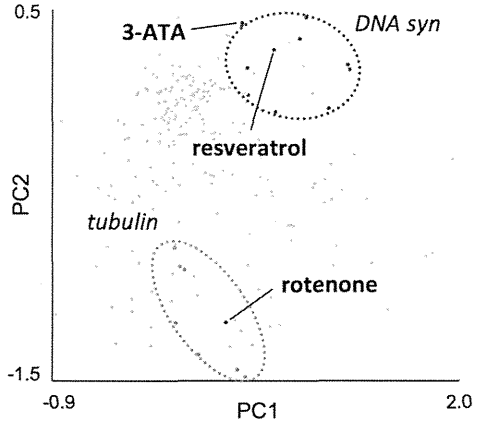

B

Rotenone			3-ATA			resveratrol		
Rank	Class	Score	Rank	Class	Score	Rank	Class	Score
1	tubulin	1.03	1	DNA	1.56	1	DNA	0.92
2	Eg5	1.92	2	ionophore	2.85	2	RNA	2.75
3	HSP60	2.13	3	RNA	4.11	3	ionophore	2.87
4	ionophore	2.26	4	V-ATPase	4.24	4	actin	3.90
5	V-ATPase	2.72	5	ctrl	4.35	5	V-ATPase	3.97
6	actin	2.87	6	Eg5	4.94	6	HSP90	4.30
7	DNA	2.91	7	actin	4.97	7	ctrl	4.37
8	PP2A	3.27	8	HSP90	5.52	8	proteasome	4.48
9	proteasome	3.58	9	protein	5.62	9	Eg5	4.63
10	HSP90	4.34	10	proteasome	5.81	10	protein	4.92
11	HDAC	4.84	11	tubulin	6.47	11	HSP60	5.38
12	RNA	5.43	12	HDAC	7.29	12	tubulin	6.41
13	protein	5.74	13	HSP60	7.64	13	HDAC	6.89
14	ctrl	5.89	14	PP2A	9.80	14	TOP2 cat	6.98
15	TOP2 cat	8.41	15	TOP2 cat	11.96	15	PP2A	9.42

Figure 5. Target Profiling of Rotenone, 3-ATA, and Resveratrol by Using Morphobase

src^{ts}-NRK and HeLa cells were treated with rotenone, 3-ATA, or resveratrol, and the obtained phenotype multiparameters were subjected to Morphobase analysis. Target prediction was carried out based on probability scores and similarity ranks, determined by Euclidean distance metrics.

(A) PCA scores of rotenone, 3-ATA, and resveratrol were projected onto 2D scatterplots of PC1 and PC2.

(B) Ranking of the likely modes of action for these compounds among 14 target classes in the training set is shown.

See also Table S3.

phase increased by concentration (Figure S2). Similar results were obtained with the other compounds, suggesting that these active substances affect G2/M phase events.

To detail the mechanism of action of these compounds, we performed Morphobase profiling. Following treatment with NPD6689, NPD8617, and NPD8969 at the concentrations in Table S1, nuclei were stained, and the resulting morphological changes were quantified by IN Cell Analyzer. The obtained phenotypic multiparameters were compared with the reference data set and subjected to statistical analysis. On projecting the samples' PCA scores, the phenotypic responses of NPD6689, NPD8617, and NPD8969 were similar to each other and formed a cluster around tubulin inhibitors in the scatterplots (Figure 6A). In addition, based on the similarity analysis, NPD6689 was predicted to perturb microtubule dynamics ($Score_{tubulin}$ = 1.06), and most of its 20 closest neighbors were typical microtubule inhibitors (Figure 6B; Table S4). Similar results were obtained for NPD8617 and NPD8969, indicating that the molecular target of these compounds is the microtubule system.

To verify these predictions, the compounds were subjected to proteome profiling. The proteomic variation of 296 spots that matched on all gel images was quantified, and hierarchical cluster analysis was performed as described (Muroi et al., 2010). Consistent with the Morphobase profiling, they were clustered with typical microtubule-targeting inhibitors and near the TOP2 catalytic inhibitors, such as BNS22 and ICRF193 (Figure S3).

The mechanism of action with regard to the microtubule system was confirmed by in vitro microtubule assembly assay. All three compounds inhibited the polymerization of tubulin dose dependently (Figures 6C and S4A). Furthermore, these effects were visualized in intact cells by immunofluorescence.

Table 1. Growth Inhibitory Effects of NPD6689, NPD8617, and NPD8969 in Various Cancer Cell Lines

	IC_{50} (μM)		
Cell Line	NPD6689	NPD8617	NPD8969
A549	1.7	0.4	1.1
HeLa	0.6	0.2	0.2
HL-60	1.7	0.2	1.6
HT1080	2.0	0.2	0.5
Jurkat	0.6	0.1	0.2
MG-63	0.9	0.2	0.5
Saos-2	2.7	0.3	2.1
src^{ts}-NRK	4.1	0.7	0.7

See also Figure S2.

After a 12 hr treatment, NPD6689 and NPD8617/NPD8969 effected microtubule depolymerization, causing short microtubule fragments to scatter throughout the cytoplasm as vinblastine treatment (Figures 6D and S4B). The effects that approximated those of TOP2 catalytic inhibitors were excluded due to the lack of distorted spindles and the failure of chromosomal alignment and segregation. These data suggest that NPD6689, NPD8617, and NPD8969 inhibit microtubule integrity in cell-free and cell-based systems.

DISCUSSION

The discovery of novel bioactive substances has become routine; however, one must judge immediately if their activities in a primary screening can be advanced to the drug development stage. Thus, the approximate mode of action must be determined to select the compounds that selectively attack tumors, and the speed of identification will save time and avoid unnecessary efforts from being made. It has been known that experienced cell biologists can judge the presumed mechanism of action of a test compound properly by the simple observation of typical morphological changes in treated cells. So far, several morphology-based assay systems, using mammalian cells, filamentous fungi, and yeasts, have been developed, some of which have successfully led to the discovery of unique drugs and probes (Frost et al., 1995; Gunji et al., 1983). In addition, the accumulated knowledge on phenotypic data can help us avoid the same mistakes repeatedly. For instance, we have developed an in-house phenotype evaluation system, using K562 cells (Osada et al., 1988), HL-60 cells, SHSY-5Y cells, tsFT210 cells (Osada et al., 1997), and *src*^{ts}-NRK cells, which was effectively utilized for the discovery of novel microbial metabolites (Kakeya et al., 1995) and to discriminate typical ones: PKC inhibitors, such as staurosporine and K252a (blebbing in K562 cells); tumor promoters, such as teleocidins and TPA (differentiation of HL-60 cells; Huberman and Callaham, 1979); and protein synthesis inhibitors (flat reversion of *src*^{ts}-NRK cells; Osada et al., 1991). However, such know-how is just empirical—there is obvious lack of consensus on morphological changes, partly due to a skill shortage, interobserver variability, and the differences of the cell lines and test compounds between laboratories—which often leads to inconclusive results and delays in the wide application of this method.

While screening for a compound that reverts the morphology of *src*^{ts}-NRK cells, we observed that vinblastine induced a notable phenotype (Figure 1). We also noticed that when treated with other chemicals, these cells experienced an endless variety of changes in shape, prompting us to record the phenotypes of *src*^{ts}-NRK cells that were induced by various compounds and classify these changes by certain rules. As expected, the cytoskeletal modulators of tubulin and actin dynamics induced characteristic morphological changes that were associated with their respective targets. Notably, the other drugs, such as inhibitors of macromolecule synthesis, HSP, or HDAC inhibitors, whose effects are unrelated to the cytoskeleton, also induced the unique alternations in morphology. The cross-validation of phenotypic responses between *src*^{ts}-NRK and HeLa cells has the following advantage: for either cell line, it was difficult to recognize certain phenotypes, such as those induced by HDAC and proteasome inhibitors in *src*^{ts}-NRK cells (flattened), and protein or RNA synthesis inhibitors in HeLa cells (toxic/growth inhibition). However, with phenotype response data for two distinct cell lines, we could discriminate them easily. Another advantage is the increase in number of compounds that can be analyzed; because drug sensitivity depends on cell types, by using two different cell lines, we could validate the phenotype of a drug that could not be visualized in either cell line in individual assays. Finally, we could easily discern the 13 types of phenotypes that were induced by typical anticancer drugs (Figure 1). Few studies have reported the systematic collection of the morphological changes that are induced by drugs in intact mammalian cells or their chemical-genetic classification (Sumiya et al., 2011), due to the limited number of phenotypic changes observed in the cells used. Our observations on the *src*^{ts}-NRK cell line revealed their potential to react to external signals with a wide variety of the morphological changes, possibly because it was transformed by oncogenic *v*-Src (Chen et al., 1977). Compared with HeLa cells, the broad spectrum of Src activities (Thomas and Brugge, 1997) might confer specific characteristics in a highly developed cytoskeletal system, enhance survival in a specific environment and against cytocidal drugs, or disrupt inherent cell-cycle checkpoints. Thus, we expect the ability to induce these changes to be coupled with many diverse classes of cellular targets. Dozens of Src-interacting proteins have been identified (Luo et al., 2008); however, the precious role of Src and the impact of its modulators on morphology remain unclear. Agents that induce unique shapes in *src*^{ts}-NRK cells are potentially useful drugs for cancer treatment or probes for better understanding of Src function and its related signal transduction.

In this report, we developed a high-content image method and a phenotype profiling system using a similarity search software, based on a statistical analysis of multiparametric phenotype responses, to identify the molecular targets of compounds of interest with an "unbiased eye." Unlike other methods (Pepperkok and Ellenberg, 2006), our system consists only of a 96-well plate, a microscope, and general fluorescent nuclear staining. Thus, this simple system allows us to select substances immediately without the pitfalls of fluorescence-based assays. Actually, in Morphobase profiling, we can distinguish between the modes

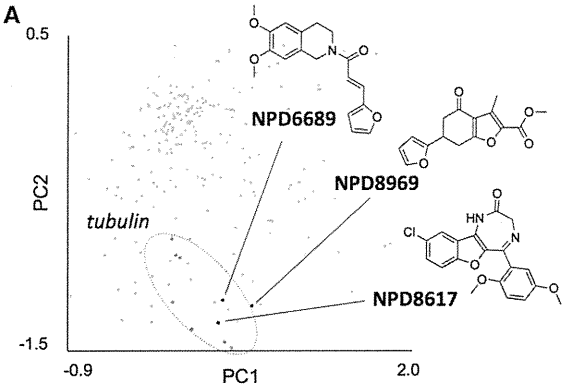

B

NPD6689		
Rank	Class	Score
1	tubulin	1.06
2	Eg5	1.94
3	DNA	3.03
4	ionophore	3.42
5	actin	3.48
6	V-ATPase	4.40
7	HSP60	4.54
8	proteasome	4.63
9	RNA	4.74
10	HSP90	4.98
11	PP2A	5.01
12	protein	5.47
13	HDAC	6.29
14	ctrl	6.53
15	TOP2 cat	10.88

NPD8617		
Rank	Class	Score
1	tubulin	1.01
2	Eg5	1.94
3	DNA	3.12
4	actin	3.54
5	ionophore	3.74
6	HSP60	4.26
7	PP2A	4.46
8	V-ATPase	4.49
9	proteasome	4.74
10	HSP90	5.04
11	RNA	5.23
12	HDAC	6.11
13	protein	6.18
14	ctrl	7.12
15	TOP2 cat	10.83

NPD8969		
Rank	Class	Score
1	tubulin	1.25
2	Eg5	2.11
3	DNA	3.08
4	actin	3.22
5	ionophore	3.73
6	proteasome	4.35
7	V-ATPase	4.38
8	HSP60	4.42
9	HSP90	4.63
10	RNA	5.27
11	PP2A	5.58
12	HDAC	6.29
13	protein	6.43
14	ctrl	7.07
15	TOP2 cat	10.21

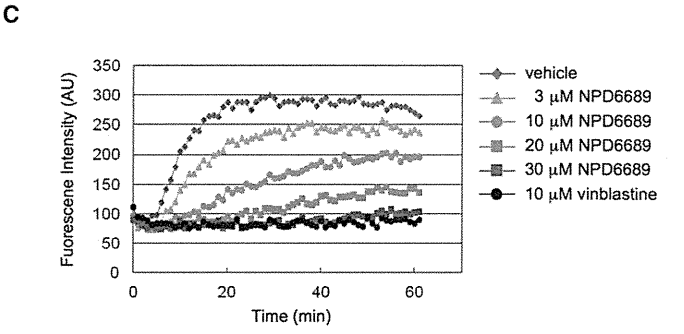

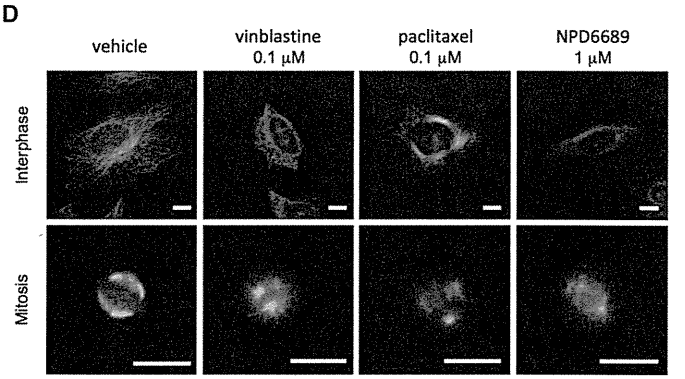

Figure 6. Target Profiling of Three Antimitotics by Using Morphobase

src^{ts}-NRK and HeLa cells were treated with NPD6689, NPD8617, or NPD8969, and the resulting phenotype multiparameters were subjected to Morphobase analysis.

(A) PCA scores for NPD6689, NPD8617, and NPD8969 were projected onto a 2D scatterplot of PC1 and PC2.

(B) Ranking of the likely mode of action among 14 target classes in the training set is shown.

(C) Effect of NPD6689 on in vitro tubulin polymerization is presented.

(D) Effect of NPD6689 on microtubules in interphase and mitotic spindle morphology is demonstrated. Cells were treated with the indicated compounds for 12 hr and stained with anti-α-tubulin (green), anti-γ-tubulin (red), and DAPI (blue). Scale bars, 10 μm.

See also Figures S2–S5 and Table S4.

of action of BNS22 and ICRF193 (TOP2 catalytic inhibitors) and etoposide (TOP2 poison), although they target the same protein, as in proteome profiling. Intriguingly, proteasome and HSP90 inhibitors or TOP2 catalytic and tubulin inhibitors lay in overlapping clusters by proteome profiling, but Morphobase profiling discriminated them clearly. Nonetheless, Morphobase suffers from a disadvantage in characterizing drugs that effect colorless morphological change, such as certain kinase inhibitors. Thus, an effective complementary combination of proteome and Morphobase profiling should be required to identify the mechanism of action more accurately.

Morphobase profiling provides us an exciting perspective for the prediction of the side effects and ancillary mechanisms of a drug. Recently, we focused on rotenone, 3-ATA, and resveratrol and identified their additional modes of action, consist with previous reports: rotenone as a tubulin inhibitor (Brinkley et al., 1974) and the latter two drugs as DNA synthesis inhibitors (Diccianni et al., 2004; Leone et al., 2010). Further characterization of the compounds that we examined in this study and those in widespread clinical practice will increase our understanding of their action mechanisms and side effects, advancing drug discovery efforts. On the contrary, drug-induced phenotypes are often changed depending on its concentration, and Morphobase mostly provided the responsible target for its growth inhibitory activity. In our future study, the assessments in primary screening will be carried out at single concentration in order to select compounds of interest from huge samples as quick as possible. Consequently, to speculate on a target, we will examine candidates' biological activities at multiple concentrations at first and then we turn into the morphological profiles.

More recently, we have identified a biosynthetic gene cluster for terpendole E and isolated several indole-alkaloid compounds from the gene-engineered strain of *Chaunopycnis alba* (Motoyama et al., 2012). Paspaline is a common key intermediate of the terpendole pathway and paxilline pathway. The molecular target of paspaline isolated from the mutant strain of *C. alba* is predicted to be Eg5 by Morphobase profiling (Figures 4 and S6A). Remarkably, the target can be predicted, even when crude extracts of the mutant strain (PQ-2) were tested (Figures S6B and 6C). These data verified the utility of our profiling system to predict various pharmacological targets of mechanistically unknown drugs and even crude natural products.

In conclusion, to discover small drug-like molecules, we developed a cell phenotype profiling system using a morphology

database, Morphobase. Our system classifies the modes of action of test compounds and predicts side and off-target effects, leading us to identify NPD6689, NPD8617, and NPD8969 as tubulin inhibitors. Currently, there are many cancer therapeutics that alter microtubule dynamics, including vinca alkaloids and taxanes. Tubulin is an old molecular target, but it remains attractive, as demonstrated by the recent FDA approval of eribulin for cancer treatment (Jain and Cigler, 2012). Although 6-furan-2-yl-3-methyl-4-oxo-4,5,6,7-tetrahydro-1*H*-indole-2-carboxylic acid derivatives that have similar chemical structures to NPD8969 have been reported as tubulin inhibitors (Screpanti et al., 2010), others are structurally unrelated to existing antitubulin agents. In addition, these antimitotics have antiproliferative activities against the vindesine- and paclitaxel-resistant H69 human small-cell lung cancer cell line (Figure S5), implicating it as a lead compound for the development of a new class of antitubulin drugs that overcome clinically evident drug resistance.

The Morphobase system rapidly groups a newly discovered compound to a class with similar mechanisms of action. With data on other cell lines, the exact molecular target can be pinpointed, based on the combination of morphological changes. Knockdown of specific genes by RNAi might provide us with exact morphological changes in the cells and improve the accuracy of the system in identifying the molecular mechanisms of drug activity and toxicity as well.

SIGNIFICANCE

To discover small drug-like molecules, we established the encyclopedic cell morphology database Morphobase, being inspired by our findings that cells dynamically and specifically alter their morphology depending on the mode of action of a drug. We examined the effects of approximately 200 well-characterized drugs on the morphological changes of intact cells in two cancer cell lines. We also prepared a custom-made image analysis algorithm to monitor cell morphology in detail and transformed an analog cell morphology database into an automated high-content database in which the phenotypes and mechanism of action of a drug are quantitatively linked in a chemical-genetic fashion. Using this database, we can easily discriminate typical anticancer drug-induced phenotypes and profile the side effects of drugs with multiple biological targets, such as rotenone. Moreover, in combination with statistic computations, we identified tubulin as the molecular target of the mechanistically unknown drugs NPD6689, NPD8617, and NPD8969 and demonstrated that these compounds inhibit microtubule dynamics in vitro and in a cell-based system.

Overall, as an alternative to current high-content approaches, we established a chemical-genetic phenotype profiling system, based on Morphobase. Our system classifies the modes of action of well-characterized compounds and predicts compounds with reported side (or off-target) effects or with unknown mechanisms. This sensitive and convenient profiling tool can determine the mechanisms of action and off-target effects of drugs and will facilitate the discovery of bioactive compounds with unknown mechanisms of action.

EXPERIMENTAL PROCEDURES

Compounds

Authentic compounds and the chemical library were provided by the RIKEN NPDepo (Osada, 2010) and SCADS inhibitor kits (Kong et al., 2010). The origins of all compounds used to construct Morphobase are summarized in Table S1. The purity and structure of each hit compound were confirmed by spectral analysis; only NPD6689, due to its low purity, was prepared by chemical synthesis (see also Supplemental Experimental Procedures).

Cell Culture

src^{ts}-NRK cells (Chen et al., 1977), rat kidney cells that were infected with ts25, a T class mutant of Rous sarcoma virus Prague strain (gifted from Dr. Y. Uehara), were cultured at permissive temperature (32°C) in Eagle's minimal essential medium (EMEM; Sigma-Aldrich), supplemented with 10% calf serum (CS; Nichirei). The human cervix epidermoid carcinoma cell line HeLa, the human fibrosarcoma cell line HT1080, and the human lung adenocarcinoma cell line A549 were cultured in Dulbecco's modified Eagle's medium (DMEM; Invitrogen), supplemented with 10% fetal bovine serum (FBS, Nichirei). The human small-cell lung cancer cell line H69, vindesine-resistant (H69/VDS) and paclitaxel-resistant cell lines (H69/Txl) (gifted from Dr. F. Koizumi) (Yoshida et al., 2007), the human promyelocytic leukemia cell line HL-60, and the human T lymphocyte cell line Jurkat were cultured in RPMI-1640 medium (Invitrogen), supplemented with 10% FBS. The human osteosarcoma cell line MG-63 was cultured in EMEM, supplemented with 10% FBS. The human osteosarcoma cell line Saos-2 was cultured in McCoy's (Invitrogen), supplemented with 10% FBS. All cell lines except for *src*^{ts}-NRK and H69 were obtained from RIKEN Cell Bank.

Image Acquisition and Analysis

src^{ts}-NRK cells (1×10^4 cells/well in 100 μl EMEM) and HeLa cells (4×10^3 cells/well in 100 μl DMEM) were plated on poly-D-lysin-coated, black, 96-well clear-bottom plates (Bio-One μclear; Greiner). After a 48 or 24 hr exposure to a test compound for *src*^{ts}-NRK or HeLa cells, respectively, the cells were fixed by direct addition of 100 μl 7.4% formalin and 2 μg/ml Hoechst 33342 (Sigma-Aldrich) in PBS and were incubated for 1 hr at room temperature. Bright-field images and corresponding nuclear images were acquired on an IN Cell Analyzer 2000 (GE Healthcare) using a ×40 objective (NA 0.45), a 12-bit camera with 1 × 1 pixel binning, and a laser autofocus system until 1,500 cells were analyzed in each well. Unanalyzable images—such as those with a tiny scratch on the plates or floc—were removed, and the remaining images, consisting of approximately 1,000 cells, were analyzed with custom-designed image analysis algorithms that were created with IN Cell Developer Toolbox as follows:

Step 1: "Nuclear" segmentation. Nuclear-stained images were segmented using the objective segmentation module. Postprocessing nodes, such as dilation, erosion, and sieve, were used to separate close nuclei and properly segment the diverse nuclear phenotypes.
Step 2: "Cell" segmentation. First, preprocessing (inversion of intensity of bright-field images) and removal of tiny objects that were irrelevant to cell shape were performed. Then, "Cell center" was predefined as a seed region of cell contour using the objective segmentation module and postprocessing nodes and allocating nuclei to respective cells. "Cell" was defined as the cellular regions that corresponded to "Cell center" by the objective segmentation module.
Step 3: Granular segmentation. The invert images above and pseudofluorescence images that were generated from bright-field images were used to detect textures, such as granules and vesicles, which were recognized by the vesicle segmentation module.
Step 4: Measure nodes. After individual cells were segmented, 12 user-defined descriptors (nuclear area, nuclear perimeter, nuclear form factor, nuclear major/minor axis length, nuclear count, nuclear intensity, cell area, cell perimeter, cell major/minor axis length, cell form factor, granular counts, and granular area) were calculated for each cell.

Statistical Analysis

Data Processing, Normalization, and PCA

To characterize well-level phenotypic responses, the average, median, and SD of each parametric measurement were calculated. Because the median

nuclear count of HeLa cells was constant (i.e., 1) regardless of treatment, 71 parameters (12 parameters × 3 statistics × 2 cells − 1 statistics) were normalized to the average corresponding control values of the DMSO-treated cells; common logarithmic outputs (x_j) were then applied to the subsequent statistical analysis. For PCA, The eigenvalue-eigenvector of the covariance matrix was calculated, and the resulting principal component scores were displayed in a 2D scatterplot.

Target Estimation by Morphobase Profiling

The prediction of a target molecule or mechanism of action of a test drug was demonstrated by using two statistical computations:

(1) Probability scores. First, we calculated the coordinate of the median point ($a_i = (a_{i1}, a_{i2} \ldots a_{in})$) and the SD ($s_i = (s_{i1}, s_{i2} \ldots s_{in})$) for each well-characterized "$Target_i$" as a training data set. To predict a compound's mechanism of action, a parameter, termed "probability score," was derived, according to

$$Score_i = \sqrt{\frac{\sum_{j=1}^{n}\left(\frac{x_j - a_{ij}}{s_{ij}}\right)^2}{n}},$$

where x_j is the coordinate of the test compound, and n is the number of the parameter. If $Score_i = 0$, the compound lies at the median point of $Target_i$. If probability $Score_i = 1$, it lies on the hyperplane that forms from the median point and SD of $Target_i$: A smaller score reflects a greater probability.

(2) The ranking of the nearest neighbors to a test compound. The similarity is determined by Euclidean distance between selected compound and reference compounds: smaller distance reflects closer phenotypic readouts to the test compound. We can assign test compound to the class to which most of its nearest neighbors belong.

In Vitro Tubulin Polymerization Assay

In vitro tubulin polymerization assay was performed using the Tubulin Polymerization Assay Kit (Cytoskeleton) per the manufacturer's instructions. Briefly, lyophilized porcine tubulin was solubilized to a final concentration of 2 mg/ml in reaction buffer, containing 80 mM PIPES (pH 6.9), 2 mM $MgCl_2$, 0.5 mM EGTA, 1 mM GTP, 10 μM fluorescent reporter, and 20% glycerol, and kept at 4°C. Compounds, (100 × DMSO stock solutions) were added to prewarmed half-area 96-well black plates. Cold tubulin solution was added to the wells, the plate contents were mixed by shaking, and the absorbance at 340 nm was read every minute for 1 hr.

Immunofluorescence Cell Staining

For α-tubulin and γ-tubulin costaining, cells were fixed in ice-cold methanol for 5 min and washed with PBS. After being blocked with 0.5% BSA in PBS for 5 min at room temperature, the slides were incubated sequentially with primary antibodies, each diluted 1:200 in PBS with 0.5% BSA, for 1 hr at 37°C and Alexa-conjugated secondary antibodies, each diluted 1:500 in PBS with 0.5% BSA, for 40 min at 37°C. Cells were also counterstained with DAPI to visualize the nuclei. Images were acquired on a fluorescence microscope (PROVIS AX70; Olympus). The primary antibodies were mouse monoclonal anti-α-tubulin and rabbit polyclonal anti-γ-tubulin (Sigma-Aldrich); the secondary antibodies were Alexa 488 goat anti-mouse IgG and Alexa 546 goat anti-rabbit IgG (Molecular Probes).

SUPPLEMENTAL INFORMATION

Supplemental Information includes six figures, four tables, and Supplemental Experimental Procedures and can be found with this article online at http://dx.doi.org/10.1016/j.chembiol.2012.10.014.

ACKNOWLEDGMENTS

We thank Y. Uehara (Iwate Medical University) for kindly providing src^{ts}-NRK cells, F. Koizumi (National Cancer Center Research Institute) for providing H69, H69/VDS, and H69/Txl cells, J. Kobayashi (Hokkaido University) for providing iejimalide A, and H. Nakamura (Gakushuin University) for providing GN26361 and mizoribine. The SCADS inhibitor kits were a kind gift of the Screening Committee of Anticancer Drugs supported by a Grant-in-Aid for Scientific Research on Innovative Areas, Scientific Support Programs for Cancer Research from MEXT. We also thank H. Aono, Y. Fukushima, K. Noda, and H. Kondo for technical assistance, K. Wierzba and T. Motoyama for critical review of the manuscript, and members of RIKEN NPDepo for the chemical libraries. This work was supported in part by a Special Postdoctoral Research Program of RIKEN, Grant-in-Aid for Scientific Research (KAKENHI), Health and Labour Sciences Research Grant, and the Program for Promotion of Basic and Applied Researches for Innovations in Bio-oriented Industry.

Received: July 18, 2012
Revised: October 19, 2012
Accepted: October 23, 2012
Published: December 20, 2012

REFERENCES

Abassi, Y.A., Xi, B., Zhang, W., Ye, P., Kirstein, S.L., Gaylord, M.R., Feinstein, S.C., Wang, X., and Xu, X. (2009). Kinetic cell-based morphological screening: prediction of mechanism of compound action and off-target effects. Chem. Biol. *16*, 712–723.

Brinkley, B.R., Barham, S.S., Barranco, S.C., and Fuller, G.M. (1974). Rotenone inhibition of spindle microtubule assembly in mammalian cells. Exp. Cell Res. *85*, 41–46.

Chen, Y.C., Hayman, M.J., and Vogt, P.K. (1977). Properties of mammalian cells transformed by temperature-sensitive mutants of avian sarcoma virus. Cell *11*, 513–521.

Diccianni, M.B., Yu, J., Meppelink, G., de Vries, M., Shao, L., Gebauer, S., Shih, H., Roberts, W., Kilcoin, N.P., Pullen, J., et al. (2004). 3-amino thioacridone inhibits DNA synthesis and induce DNA damage in T-cell acute lymphoblastic leukemia (T-ALL) in a p16-dependent manner. J. Exp. Ther. Oncol. *4*, 223–237.

Feng, Y., Mitchison, T.J., Bender, A., Young, D.W., and Tallarico, J.A. (2009). Multi-parameter phenotypic profiling: using cellular effects to characterize small-molecule compounds. Nat. Rev. Drug Discov. *8*, 567–578.

Fenteany, G., Standaert, R.F., Lane, W.S., Choi, S., Corey, E.J., and Schreiber, S.L. (1995). Inhibition of proteasome activities and subunit-specific amino-terminal threonine modification by lactacystin. Science *268*, 726–731.

Frémont, L. (2000). Biological effects of resveratrol. Life Sci. *66*, 663–673.

Frost, D.J., Brandt, K.D., Cugier, D., and Goldman, R. (1995). A whole-cell *Candida albicans* assay for the detection of inhibitors towards fungal cell wall synthesis and assembly. J. Antibiot. (Tokyo) *48*, 306–310.

Gunji, S., Arima, K., and Beppu, T. (1983). Screening of antifungal antibiotics according to activities inducing morphological abnormalities. Agric. Biol. Chem. *47*, 2061–2069.

Houle, D., Govindaraju, D.R., and Omholt, S. (2010). Phenomics: the next challenge. Nat. Rev. Genet. *11*, 855–866.

Huberman, E., and Callaham, M.F. (1979). Induction of terminal differentiation in human promyelocytic leukemia cells by tumor-promoting agents. Proc. Natl. Acad. Sci. USA *76*, 1293–1297.

Jain, S., and Cigler, T. (2012). Eribulin mesylate in the treatment of metastatic breast cancer. Biologics *6*, 21–29.

Kakeya, H., Takahashi, I., Okada, G., Isono, K., and Osada, H. (1995). Epolactaene, a novel neuritogenic compound in human neuroblastoma cells, produced by a marine fungus. J. Antibiot. (Tokyo) *48*, 733–735.

Kawatani, M., Takayama, H., Muroi, M., Kimura, S., Maekawa, T., and Osada, H. (2011). Identification of a small-molecule inhibitor of DNA topoisomerase II by proteomic profiling. Chem. Biol. *18*, 743–751.

Kong, D., Yamazaki, K., and Yamori, T. (2010). Discovery of phosphatidylinositol 3-kinase inhibitory compounds from the Screening Committee of Anticancer Drugs (SCADS) library. Biol. Pharm. Bull. *33*, 1600–1604.

Kubo, A., Nakagawa, K., Varma, R.K., Conrad, N.K., Cheng, J.Q., Lee, W.C., Testa, J.R., Johnson, B.E., Kaye, F.J., and Kelley, M.J. (1999). The p16

status of tumor cell lines identifies small molecule inhibitors specific for cyclin-dependent kinase 4. Clin. Cancer Res. *5*, 4279–4286.

Leone, S., Cornetta, T., Basso, E., and Cozzi, R. (2010). Resveratrol induces DNA double-strand breaks through human topoisomerase II interaction. Cancer Lett. *295*, 167–172.

Luo, W., Slebos, R.J., Hill, S., Li, M., Brábek, J., Amanchy, R., Chaerkady, R., Pandey, A., Ham, A.J., and Hanks, S.K. (2008). Global impact of oncogenic Src on a phosphotyrosine proteome. J. Proteome Res. *7*, 3447–3460.

MacDonald, M.L., Lamerdin, J., Owens, S., Keon, B.H., Bilter, G.K., Shang, Z., Huang, Z., Yu, H., Dias, J., Minami, T., et al. (2006). Identifying off-target effects and hidden phenotypes of drugs in human cells. Nat. Chem. Biol. *2*, 329–337.

Motoyama, T., Hayashi, T., Hirota, H., Ueki, M., and Osada, H. (2012). Terpendole E, a kinesin Eg5 inhibitor, is a key biosynthetic intermediate of indole-diterpenes in the producing fungus *Chaunopycnis alba*. Chem. Biol. *19*, this issue, 1611–1619.

Muroi, M., Kazami, S., Noda, K., Kondo, H., Takayama, H., Kawatani, M., Usui, T., and Osada, H. (2010). Application of proteomic profiling based on 2D-DIGE for classification of compounds according to the mechanism of action. Chem. Biol. *17*, 460–470.

Ohnuki, S., Oka, S., Nogami, S., and Ohya, Y. (2010). High-content, image-based screening for drug targets in yeast. PLoS One *5*, e10177.

Omura, S., Fujimoto, T., Otoguro, K., Matsuzaki, K., Moriguchi, R., Tanaka, H., and Sasaki, Y. (1991). Lactacystin, a novel microbial metabolite, induces neuritogenesis of neuroblastoma cells. J. Antibiot. (Tokyo) *44*, 113–116.

Osada, H. (2010). Introduction of new tools for chemical biology research on microbial metabolites. Biosci. Biotechnol. Biochem. *74*, 1135–1140.

Osada, H., Magae, J., Watanabe, C., and Isono, K. (1988). Rapid screening method for inhibitors of protein kinase C. J. Antibiot. (Tokyo) *41*, 925–931.

Osada, H., Koshino, H., Isono, K., Takahashi, H., and Kawanishi, G. (1991). Reveromycin A, a new antibiotic which inhibits the mitogenic activity of epidermal growth factor. J. Antibiot. (Tokyo) *44*, 259–261.

Osada, H., Cui, C.B., Onose, R., and Hanaoka, F. (1997). Screening of cell cycle inhibitors from microbial metabolites by a bioassay using a mouse cdc2 mutant cell line, tsFT210. Bioorg. Med. Chem. *5*, 193–203.

Pepperkok, R., and Ellenberg, J. (2006). High-throughput fluorescence microscopy for systems biology. Nat. Rev. Mol. Cell Biol. *7*, 690–696.

Perlman, Z.E., Slack, M.D., Feng, Y., Mitchison, T.J., Wu, L.F., and Altschuler, S.J. (2004). Multidimensional drug profiling by automated microscopy. Science *306*, 1194–1198.

Roti, G., and Stegmaier, K. (2012). Genetic and proteomic approaches to identify cancer drug targets. Br. J. Cancer *106*, 254–261.

Screpanti, E., Santaguida, S., Nguyen, T., Silvestri, R., Gussio, R., Musacchio, A., Hamel, E., and De Wulf, P. (2010). A screen for kinetochore-microtubule interaction inhibitors identifies novel antitubulin compounds. PLoS One *5*, e11603.

Sumiya, E., Shimogawa, H., Sasaki, H., Tsutsumi, M., Yoshita, K., Ojika, M., Suenaga, K., and Uesugi, M. (2011). Cell-morphology profiling of a natural product library identifies bisebromoamide and miuraenamide A as actin filament stabilizers. ACS Chem. Biol. *6*, 425–431.

Takahashi, H., Osada, H., Koshino, H., Sasaki, M., Onose, R., Nakakoshi, M., Yoshihama, M., and Isono, K. (1992). Reveromycins, new inhibitors of eukaryotic cell growth. II. Biological activities. J. Antibiot. (Tokyo) *45*, 1414–1419.

Thomas, S.M., and Brugge, J.S. (1997). Cellular functions regulated by Src family kinases. Annu. Rev. Cell Dev. Biol. *13*, 513–609.

Uehara, Y., Hori, M., Takeuchi, T., and Umezawa, H. (1986). Phenotypic change from transformed to normal induced by benzoquinonoid ansamycins accompanies inactivation of p60src in rat kidney cells infected with Rous sarcoma virus. Mol. Cell. Biol. *6*, 2198–2206.

Whitesell, L., Mimnaugh, E.G., De Costa, B., Myers, C.E., and Neckers, L.M. (1994). Inhibition of heat shock protein HSP90-pp60v-src heteroprotein complex formation by benzoquinone ansamycins: essential role for stress proteins in oncogenic transformation. Proc. Natl. Acad. Sci. USA *91*, 8324–8328.

Yoshida, M., Matsui, Y., Ikarashi, Y., Usui, T., Osada, H., and Wakasugi, H. (2007). Antiproliferating activity of the mitotic inhibitor pironetin against vindesine- and paclitaxel-resistant human small cell lung cancer H69 cells. Anticancer Res. *27*, 729–736.

The Journal of Antibiotics (2013) 66, 247–250

www.nature.com/ja

NOTE

Creation of novel reveromycin derivatives by alcohol-added fermentation

Toshihiko Nogawa[1], Shunji Takahashi[1], Yasuyo Sekiyama[2], Hiroshi Takagi, Masakazu Uramoto, Hiroyuki Koshino, Makoto Kawatani, Takeshi Shimizu and Hiroyuki Osada

The Journal of Antibiotics (2013) **66**, 247–250; doi:10.1038/ja.2012.115; published online 12 December 2012

Keywords: alcohol-added fermentation; reveromycins; *Streptomyces*; structure elucidation

Reveromycin A, a polyketide compound with a distinctive spiroacetal core structure (Figure 1), was isolated from *Streptomyces reveromyceticus* SN-593 as an inhibitor of epidermal growth factor-induced mitogenic activity.[1] It has various functions,[2–6] and its robust anti-osteoclastic activity[7–10] is its most prominent feature as a drug lead. To generate reveromycin derivatives that have greater activity, we recently identified a biosynthetic gene cluster of reveromycin A by gene disruption and complementation analysis.[11] We identified reveromycin T as be the biosynthetic intermediate of reveromycin A in feeding experiments.[11] To determine the biosynthetic origin of polyketide carbon sources of reveromycin A, we also fed [^{13}C]acetate and [^{13}C]propionate dissolved in alcohol. During the purification of ^{13}C-incorporated species, we observed an unexpected compound using a photodiode array detector that was attached to an LC/MS instrument and speculated it to be a novel reveromycin derivative. In this study, to identify the structure of this compound, we performed large-scale fermentation of *S. reveromyceticus* SN-593 in the presence of methanol. In addition, ethanol-added fermentation was performed, resulting in the production of another novel reveromycin derivative. Based on these experiments, two new reveromycin derivatives were isolated and determined to be reveromycin T 1-methyl ester (**1**) and 1-ethyl ester (**2**) by spectroscopic and chemical method. We report the creation of these novel derivatives and their structures, which have activities against cancer cell lines.

S. reveromyceticus SN-593 was precultured in a cylindrical flask that contained 70 ml of SK2 medium (1.4% starch, 0.35% glucose, 0.35% yeast extract, 0.21% bacto-peptone, 0.21% meat extract and 0.014% KH_2PO_4, 0.042% $MgSO_4 \cdot 7H_2O$) for 72 h at 28 °C on a rotary shaker at 150 r.p.m. One milliliter of the seed culture was transferred to cylindrical flasks that contained 70 ml of reveromycin production medium (2% potato dextrose, 1% malt extract, 1% dried yeast, 5% TABLE LAND tomato juice, 0.1% K_2HPO_4, 0.1% NaCl, 0.03% $MgSO_4 \cdot 7H_2O$, 0.01% $NaNO_3$, 0.005% $ZnSO_4 \cdot 7H_2O$ and 0.005% $CuSO_4 \cdot 5H_2O$) and cultured under the same conditions. After 72 h, 0.7 ml methanol or ethanol was added to a flask, which was cultured further for 48 h. A control culture that lacked alcohol was prepared under the same conditions. The culture broth was extracted with ethyl acetate and analyzed by photodiode array detector-LC/MS. The unidentified peaks were observed on the UV chromatograms at 238 nm for the methanol- and ethanol-added culture broths, in which reveromycin A production decreased to ~60%, as shown in Figure 2. These peaks were determined to be reveromycin derivatives, with typical UV absorption spectra for reveromycins with a λ_{max} value of ~240 nm by photodiode array detector analysis.[1] The molecular weights for peaks 1 and 2 were 558 (*m/z*: 557 [M-H]$^-$) and 572 (*m/z*: 571 [M-H]$^-$) by electrospray ionization tandem MS analysis in the negative mode, respectively, suggesting that they are methyl or ethyl derivatives of reveromycin T[11] that have not been isolated. To isolate them, 5.0 and 1.4 l fermentation cultures were begun for the addition of methanol and ethanol, respectively. The methanol-added fermentation broth yielded 5.47 g of ethyl acetate extract, which was separated by C_{18}-HPLC to obtain **1** as a colorless oil (81.1 mg). Colorless oil; $[\alpha]_{589}^{27}$-133 (c 0.15, MeOH); UV (MeOH) λ_{max} (log ε) 240 (4.58), 265 (4.24, sh) nm; ^{1}H NMR and ^{13}C NMR data, see Table 1; HR electrospray ionization *m/z*: 557.3440 [M-H]- (calcd $C_{33}H_{51}O_7$, 557.3478). The ethanol-added fermentation broth generated 1.2 g of ethyl acetate extract, which was subjected to SiO_2 flash column chromatography, C_{18}-HPLC and preparative TLC to obtain **2** as a colorless oil (12 mg). Colorless oil; $[\alpha]_D^{27}$-155 (c 0.4, MeOH); UV (MeOH) λ_{max} (log ε) 238 (4.85), 264 (4.57, sh) nm; ^{1}H NMR and ^{13}C NMR data, see Table 1; HR fast atom bombardment MS *m/z*: 571.3638 [M-H]- (calcd $C_{34}H_{53}O_7$, 571.3635).

The molecular formula of compound **1** was determined to be $C_{33}H_{50}O_7$ by HR electrospray ionization MS. The ^{1}H NMR spectrum

Chemical Biology Core Facility, Chemical Biology Department, Advanced Science Institute, RIKEN, Saitama, Japan
[1]These authors contributed equally to this work.
[2]Current address: National Food Research Institute, NARO, 2-1-12 Kannondai, Tsukuba, Ibaraki 305-8642, Japan
Correspondence: Dr H Osada, Chemical Biology Core Facility, Chemical Biology Department, Advanced Science Institute, RIKEN, Hirosawa 2-1, Wako, Saitama 351-0198, Japan.
E-mail: hisyo@riken.jp
Received 17 October 2012; revised 9 November 2012; accepted 12 November 2012; published online 12 December 2012

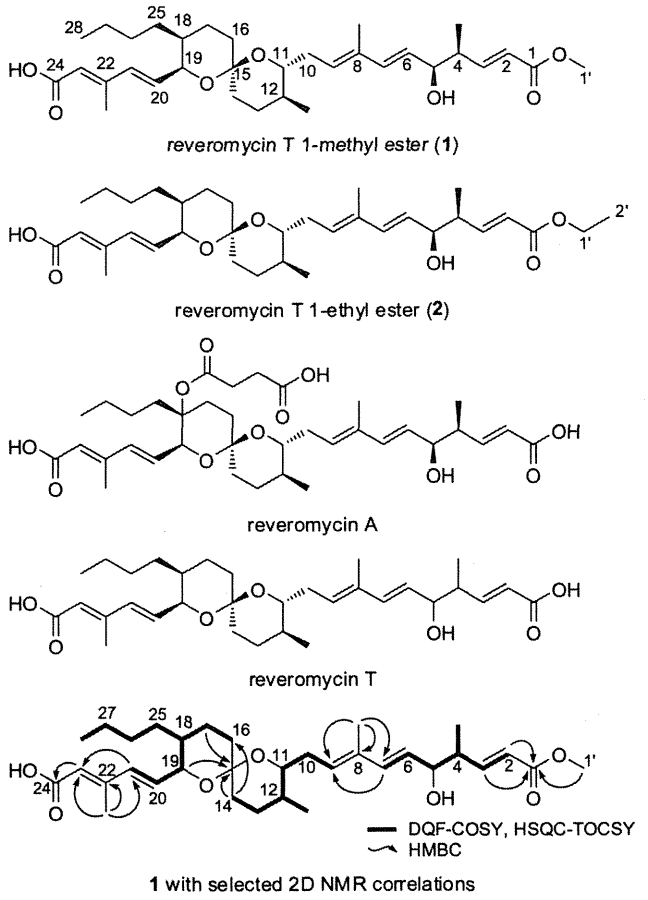

Figure 1 Structures of reveromycin derivatives.

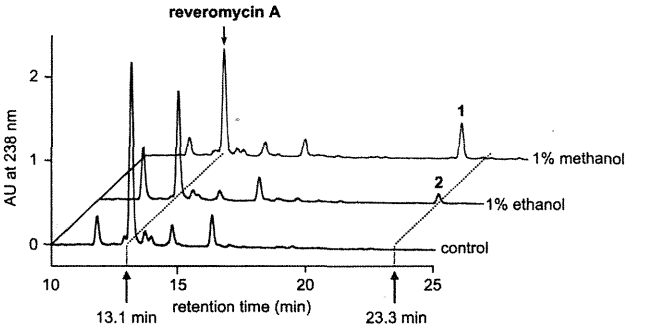

Figure 2 UV chromatograms of alcohol-added fermentation broth.

showed five methyl signals and a methoxy signal at 3.69 p.p.m. (Supplementary Figure S1). It also showed eight olefinic proton signals and three signals that were attached to oxygenated carbons. Analysis of the ^{13}C NMR and HSQC data confirmed that **1** possessed 33 carbon atoms, including 2 carbonyl carbons and a methoxy carbon, among which 3 sp^3 methines were assigned to carbon atoms that bore an oxygen atom (Supplementary Figures S2 and S5). In addition, 1 sp^3 acetal carbon signal at 97.2 p.p.m. was observed, indicating that **1** had a 6,6-spiroacetal structure.[12] The ^{13}C NMR spectra also showed 10 olefin signals, suggesting the presence of five double bonds. These observations, in conjunction with the UV absorption spectrum and molecular formula, implied that **1** is a reveromycin derivative with an additional methoxy group and the absence of a succinyl group compared with reveromycin A. Its planar structure was elucidated by analysis of the 2D NMR data, as shown in Figure 1. The DQF-COSY and HSQC-TOCSY spectra revealed three spin systems from C-2 to C-7 with a methyl branch at C-4, C-9 to C-14 with a methyl branch at C-12, and C-16 to C-21 with a butyl branch at C-18 (Supplementary Figures S3 and S4). The connections between the spin systems were established by long-range correlations in the HMBC spectrum (Supplementary Figure S6), and the overall structure was established. The methoxy group was assigned to the C-1 position, based on the long-range correlations from the methoxy signal to C-1. The 6,6-spiroacetal core was confirmed, based on the HMBC correlations from H-14, H-17, and H-19 to the acetal carbon and H-14 to C-16. The geometries of the double bonds at Δ^2, Δ^6 and Δ^{20} were designated to have *E* configurations, based on the coupling constants in the ^1H NMR spectrum. The Δ^9 and Δ^{22} bonds were *E* configurations, based on the ^{13}C NMR chemical shift values of C-8-Me and C-22-Me. The absolute configuration at C-5 was determined to be *R* by the modified Mosher's method of the dimethyl ester that was converted from **1** by treatment with trimethylsilyl diazomethane.[13,14] The configuration at C-15 was determined to be *S** by the NOESY correlations between H-11/H-13, H-16axial/H-18 and H-14equatorial/H-16axial in phase-sensitive NOESY spectrum (Supplementary Figures S7 and S8). The remaining stereochemistry including absolute configuration at C-15 assigning to be *S* was deduced to be the same as that of reveromycin A, comparing its NMR chemical shifts and optical rotations[12,14] with those of spirofungins A and B.[15–18] Based on these findings, the structure of **1** was determined as shown in Figure 1.

Compound **2** had a similar ^1H NMR spectrum as **1**, except for a newly observed ethoxy signal that comprised a triplet at 1.26 p.p.m., coupled with a quartet signal at 4.16 p.p.m. and the disappearance of a methoxy signal of **1** (Supplementary Figure S9). The molecular formula was established as $C_{34}H_{52}O_7$ by HR fast atom bombardment MS, which was identical to an ethyl ester form of **1**. The planar structure was elucidated in the same manner as that of **1**, based on an analysis of 2D NMR data (Supplementary Figures S10–S14). The attachment of the ethoxy group at C-1 was determined, based on the HMBC correlation from the quartet signal to C-1. The stereochemistry was deduced to be the same as **1**, based on a comparison of NMR data, and the structure was determined as shown in Figure 1.

The cytotoxic activities of compounds **1** and **2** and reveromycin A were evaluated against HL-60 (human promyelocytic leukemia cell line), K562 (human erythromyeloblastoid leukemia cell line) and tsFT210 (mouse temperature-sensitive mutant with a defect in *cdc2*) cells. Compared with reveromycin A, compounds **1** and **2** showed improved activity, exhibiting a 2–10-fold reduction against the HL-60 and K562 cell lines, with IC_{50} values of 0.9, 2.5 for **1**; 0.2, 0.7 for **2** and 2.7, 4.9 $\mu g\,ml^{-1}$ for reveromycin A. All three compounds showed moderate activity against tsFT210 cells, with IC_{50} values of 8.2, 11.4 and 8.5 $\mu g\,ml^{-1}$ for **1**, **2** and reveromycin A, respectively. In contrast, they did not show any antibacterial effects against *Escherichia coli* up to 50 $\mu g\,ml^{-1}$.

We created and identified two new reveromycin derivatives, reveromycin T 1-methyl ester and 1-ethyl ester, by adding a small amount of related alcohol to culture broth of *S. reveromyceticus* SN-593 during the fermentation. Similar approach to create new metabolites has not been reported before, and this simple method

Table 1 ^{1}H and ^{13}C NMR chemical shifts of compounds **1** and **2** in methanol-d_4.

	1		*2*	
Position	δ_C	δ_H *(multiplicity, J in Hz)*	δ_C	δ_H *(multiplicity, J in Hz)*
1	168.7	—	168.4	
2	121.8	5.84 (dd, 15.6, 0.7)	122.3	5.83 (dd, 15.6, 1.5)
3	152.9	6.99 (dd, 15.6, 7.8)	152.7	6.98 (dd, 15.6, 7.6)
4	44.1	2.51 (m)	44.2	2.51 (m)
5	76.8	4.05 (dd, 7.3, 6.4)	76.9	4.06 (dd, 7.6, 6.6)
6	127.7	5.50 (dd, 15.6, 7.3)	127.8	5.50 (dd, 15.6, 7.6)
7	137.9	6.23 (d, 15.6)	137.9	6.24 (d, 15.6)
8	135.3	—	135.4	—
9	129.7	5.58 (t, 7.1)	129.7	5.59 (t, 7.1)
10	33.0	2.35 (m, 2H)	33.1	2.36 (m, 2H)
11	76.0	3.43 (m)	76.1	3.45 (ddd, 10.1, 4.0, 4.0)
12	34.9	1.36 (m)	34.9	1.36 (m)
13	28.7	1.44 (m, 2H)	28.8	1.46 (m, 2H)
14	37.2	1.42 ax. (m)	37.3	1.42 ax. (m)
		1.66 eq. (m)		1.66 eq. (ddd, 12.1, 3.0, 3.0)
15	97.2	—	97.2	—
16	37.5	1.53 ax. (m)	37.6	1.53 ax. (m)
		1.76 eq. (m)		1.76 eq. (m)
17	22.6	1.54 ax. (m)	22.6	1.53 ax. (m)
		1.75 eq. (m)		1.76 eq. (m)
18	39.8	1.74 (m)	39.9	1.74 (m)
19	79.2	4.24 (br dd, 9.6, 4.1)	79.3	4.23 (dd, 9.6, 4.0)
20	135.5	6.55 (dd, 15.6, 9.6)	134.8	6.51 (dd, 15.6, 9.6)
21	137.97	6.32 (d, 15.6)	138.2	6.31 (d, 15.6)
22	152.8	—	151.0	—
23	121.0	5.82 (s)	122.5	5.83 (s)
24	170.4	—	171.5	—
25	32.7	1.09 (m, 2H)	32.8	1.10 (m)
				1.13 (m)
26	30.0	1.28 (m, 2H)	30.1	1.22 (m)
				1.28 (m)
27	23.8	1.27 (m, 2H)	23.9	1.28 (m, 2H)
28	14.3	0.87 (t, 7.1, 3H)	14.4	0.87 (t, 7.1, 3H)
Me-4	15.1	1.06 (d, 6.9, 3H)	15.2	1.07 (d, 7.1, 3H)
Me-8	12.9	1.74 (s, 3H)	13.0	1.74 (s, 3H)
Me-12	18.0	0.76 (d, 6.4, 3H)	18.0	0.77 (d, 6.6, 3H)
Me-22	14.6	2.24 (d, 0.9, 3H)	14.7	2.22 (s, 3H)
1′	51.9	3.69 (s, 3H)	61.4	4.16 (q, 7.3, 2H)
2′			14.6	1.26 (t, 7.3, 3H)

1 was recored at 500 MHz for ^{1}H and 125 MHz for ^{13}C. **2** was recored at 600 MHz for ^{1}H and 150 MHz for ^{13}C.

might be applied to other metabolites to expand their diversity for structure–activity relationship study.

CONFLICT OF INTEREST

The authors declare no conflict of interest.

ACKNOWLEDGEMENTS

We thank Ms H. Aono and Ms A. Okano for biological activity tests. This work was supported in part by the Target Protein Research Program, a Grant-in-Aid for Scientific Research (B) from the Ministry of Education, Culture, Sports, Science and Technology of Japan, the Program for Promotion of Basic and Applied Researches for Innovations in Bio-oriented Industry and Health, and Labour Sciences Research Grant.

1 Osada, H., Koshino, H., Isono, K., Takahashi, H. & Kawanishi, G. Reveromycin A, a new antibiotic which inhibits the mitogenic activity of epidermal growth factor. *J. Antibiot.* **44,** 259–261 (1991).
2 Takahashi, H. *et al.* Reveromycins, new inhibitors of eukaryotic cell growth. II. Biological activities. *J. Antibiot.* **45,** 1414–1419 (1992).
3 Cui, Z., Hirata, D., Tsuchiya, E., Osada, H. & Miyakawa, T. The multidrug resistance-associated protein (MRP) subfamily (Yrs/Yor1) of *Saccharomyces cerevisiae* is important for the tolerance to a broad range of organic anions. *J. Biol. Chem.* **271,** 14712–14716 (1996).
4 Takahashi, H. *et al.* Inhibitory action of reveromycin A on TGF-α-dependent growth of ovarian carcinoma BG-1 *in vitro* and *in vivo*. *Oncol. Res.* **9,** 7–11 (1997).
5 Miyamoto, Y. *et al.* Identification of *Saccharomyces cerevisiae* isoleucyl-tRNA synthetase as a target of the G1-specific inhibitor Reveromycin A. *J. Biol. Chem.* **277,** 28810–28814 (2002).
6 Tanaka, Y. *et al.* Reveromycin A inhibits antigen receptor-mediated antigen presentation by B lymphoma cell via its effect on intracellular trafficking of the antigen. *J. Antibiot.* **55,** 904–913 (2002).

Journal of Stem Cells
Volume 7, Number 1

ISSN: 1556-8539

Induced Pluripotent Stem Cell-Derived Hepatocytes As an Alternative to Human Adult Hepatocytes

Takeshi Katsuda[1,2], Yasuyuki Sakai[2], and Takahiro Ochiya[1]
[1]Division of Molecular and Cellular Medicine,
National Cancer Center Research Institute, Tokyo, Japan
[2]Institute of Industrial Science (IIS),
The University of Tokyo, Tokyo, Japan

Abstract

Recent advances in induced pluripotent stem (iPS) cell research have attracted much attention. The ability to generate such cells from somatic cells has implications for overcoming both immunological rejection and the ethical issues associated with embryonic stem (ES) cells. Hepatocytes derived from patient-specific iPS cells offer a possible solution to the shortage of cell sources in cell replacement therapy, drug screening, and disease model. Despite such great promise, however, recent articles have questioned the viability of the therapeutic applications of iPS cells. These cells must, therefore, satisfy stringent criteria prior to practical use. The main focus of this review is a description of the current status of hepatic differentiation technology of iPS cells and a discussion of the concerns regarding the practical use of these techniques in cell replacement therapy, drug screening, and disease model. The current status of strategies for generating iPS cells and the accumulated knowledge on strategies for differentiating ES cells into hepatocytes will be summarized. We also refer to the possibility of direct conversion of adult somatic cells into functional hepatocytes.

1. Introduction

An alternative cell source for functional hepatocytes has been essential for various applications in medicine. For severe liver failures, orthotopic liver transplantation is the only effective treatment, but it is currently limited by donor shortage. This has led to the development of cell replacement therapy in the form of hepatocyte transplantation and artificial liver support devices [1,2]. However, these approaches have been confronted with the serious problem of obtaining hepatocytes in sufficient amounts and quality. Researchers in the field of drug screening have also been presented with a donor shortage problem. In drug screening, primary human hepatocytes are the

current gold-standard because they express the entire complement of drug metabolizing enzymes and transporters [3]. However, this approach is hindered by the low quality of isolated hepatocytes. Generally, isolated hepatocytes are available only from cadaveric donor livers; thus the cells largely lack quality and quantity [4]. These situations have led researchers on a quest for alternative cell sources that can generate hepatic cells with the ability to proliferate *in vitro* and that can express hepatic functions.

Human embryonic stem (ES) cells which are capable of indefinitely proliferating and differentiating into any adult cell types have, therefore, been extensively studied [5,6]. Accordingly, many reports have shown that ES cells can be differentiated into functional hepatocytes *in vivo* and *in vitro* [7]. Furthermore, ES cells exhibit another beneficial aspect, namely, that they can also serve as a cell source for modeling genetic liver diseases. Since ES cells can go through embryonic and postembryonic development, they have the possibility to recapitulate the pathology of genetic diseases. Thus, human ES cells have raised expectations among researchers and the general public alike.

However, the use of ES cells has inherent problems. Ethical controversies regarding the use of human embryos, as well as immune rejection problems following transplantation, have hindered the applications of human ES cells. In addition, despite great efforts to generate human ES cells harboring disease-specific mutations as disease models in many laboratories, this strategy has faced challenges because of the inefficient methods to genetically modify ES cells [8].

The recent breakthrough in stem cell research has opened up new possibilities for solving these issues. Yamanaka and his colleagues demonstrated that retroviral transduction of a defined set of transcription factors give rise to induced pluripotent stem (iPS) cells directly from fibroblast cultures [9,10]. After their discoveries, remarkable progress has continued at a rapid pace, raising hopes that iPS cell technology will pave the way for cell replacement therapy, drug screening, and disease model. In addition to the possibility of circumventing immune rejection and ethical issues, derivation of patient-specific iPS cells for various liver diseases implies useful platforms for drug discovery and studying the mechanisms of diseases.

One of the major hurdles for achieving these goals is to establish an efficient protocol for differentiating iPS cells to functional hepatocytes. During the past decade, a great deal of knowledge has been accumulated regarding *in vitro* differentiation of ES cells to hepatic cell lineages, and recently researchers have demonstrated that the methods gained from that knowledge is applicable to differentiation of iPS cells into hepatic cells. Moreover, hepatocytes derived from patient-specific iPS cells have been found to recapitulate key pathological features of the diseases affecting the patients from which they were derived.

In this review, we will first summarize the current status of strategies for generating iPS cells, and then overview strategies for differentiating ES cells into hepatocytes. Subsequently we will describe the latest reports on hepatic differentiation of iPS cells including patient-specific ones. We will also discuss the concerns regarding the practical use of iPS cells in cell replacement therapy, drug screening, and disease model. In the last section, we will refer to the possibility of direct conversion of somatic cells into functional hepatocytes.

2. Generation of Pluripotent Stem Cells from Somatic Cells

The discovery that mouse and human somatic cells can be reprogrammed to pluripotent stem cells has created enthusiasm for their potential applications in regenerative medicine. Takahashi and Yamanaka first reported that transduction of a defined set of transcription factors, Kruppel-like factor 4 (KLF4), Octamer 3/4 (OCT4), SRY box–containing protein 2 (SOX2), and c-Myc, gave rise to iPS cells directly from mouse fibroblasts [9]. These cells were similar to ES cells in morphology, proliferation, the expression of some ES cell marker genes, and teratoma formation. Despite the similarity, however, they were not identical to ES cells, and failed to produce adult chimeric mice. In 2007, mouse iPS cells capable of germline transmission were generated [11-13], and human iPS cells were generated from fibroblasts [10,14,15].

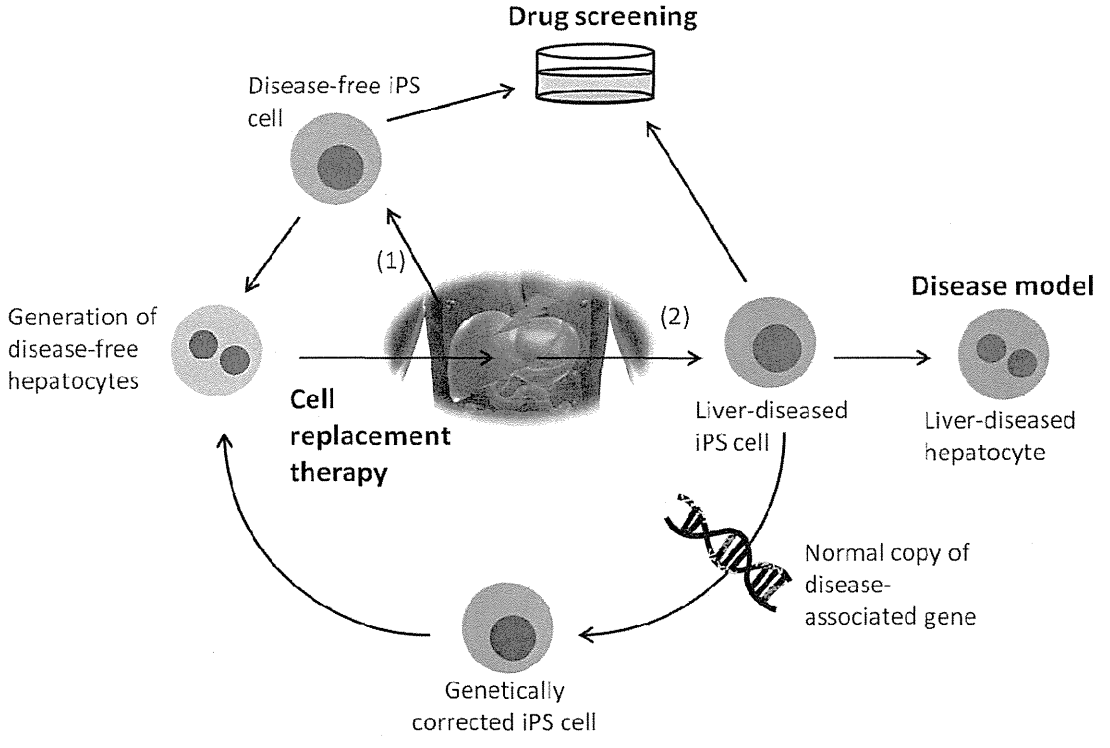

Figure 1. Possible application of patient-specific iPS cells. (1) In case of a non-genetic liver disease, generated iPS cells are disease-free, thus can be directly differentiated into hepatocytes and used for cell replacement therapy as well as drug screening. (2) In case of a genetic liver disease, reprogrammed iPS cells can be used for disease model and drug screening. For cell replacement therapy, the defect of such iPS cells should be corrected by introduction of the wild-type gene. Resultant genetically corrected iPS cells can be differentiated into hepatocytes and used for cell replacement therapy.

In the several years since those first generation iPS cells were reported, remarkable progress has continued at a rapid pace in the development of reprogramming methods. Nakagawa *et al.* generated mouse and human iPS cells without transduction of Myc, which indicated reduction of the tumorigenesis risk [16]. In 2009, Kim *et al.* generated iPS cells from mouse neural stem cells by retroviral transduction of OCT4 alone [17]. Thereafter, several reports have shown that iPS cells can be generated even without viral integration. These methods involve transient expression of reprogramming factors using plasmids [18], administration of synthetic mRNA [19], lentiviruses or transposons followed by transgene removal using Cre-mediated excision or re-expression of transposase [20,21]. As another novel strategy, several reports have shown that reprogramming factors could be replaced by identified chemicals, such as histone deacetylase inhibitors and MEK inhibitors [22,23].

Such remarkable progress has significantly implies that the generation of patient-specific iPS cells holds great promise for cell replacement therapy, drug screening, and disease model (Figure 1).

For the practical application of iPS cell technology to these fields, directly differentiating iPS cells into cell types of interest is crucial. It has already been shown that iPS cells can be differentiated *in vitro* into various cell types including neural progenitors, motor neurons, domapinergic neurons, retinal cells, adipocytes, endothelial cells, fibroblasts and hepatocytes [8]. Importantly, some of these reports involve the generation of patient-specific iPS cells, indicating promise for the future use of iPS cell technology in medicine. In the next two sections, we will focus on the generation of hepatocytes from pluripotent stem cells, namely, ES cells as well as iPS cells, and discuss the feasibility of those technologies to alternate use of human hepatocytes.

3. Overview of Generation of Hepatocytes from ES Cells

Prior to reviewing the current status of the generation of hepatocytes from iPS cells, we will overview the methodology for differentiating ES cells into hepatocytes. Theoretically, pluripotent stem cells including ES and iPS cells can precisely trace the process of *in vivo* liver development. Thus, researchers have attempted to direct these cells to hepatocytes *in vitro* by recapitulating the *in vivo* environment that hepatic precursors experience. In this section we will first mention the development of the liver. All these processes are illustrated in Figure 2. Then we will overview the representative protocols for differentiating ES cells to hepatocytes.

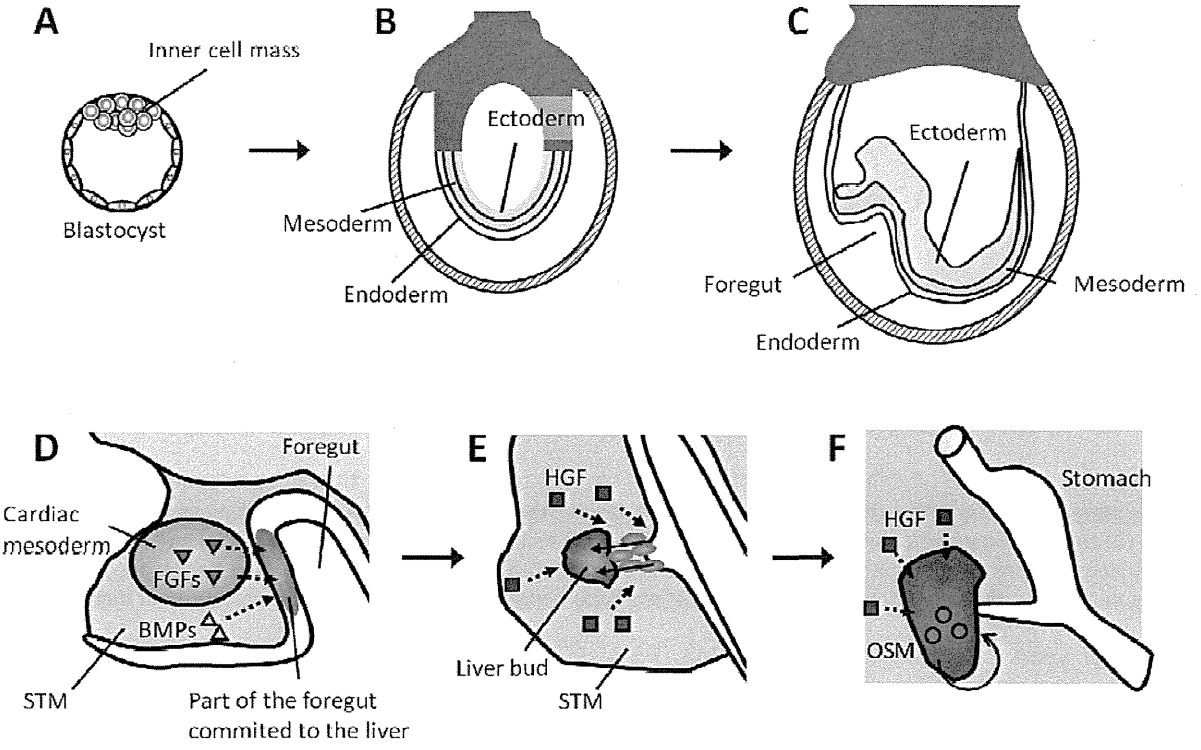

Figure 2. Summary of liver development. (A) The blastocyst harbors the inner cell mass that derives ES cells. (B) During late postimplantation, the epiblast gives rise to three germ layers — ectoderm, mesoderm, and endoderm. (C) The foregut is formed under the regulation of transcription factors such as FOXA2 and GATA4. (D) Part of the foregut generates the liver bud, the primordial diverticulum that gives rise to the liver parenchyma. FGFs from the cardiac mesoderm and BMPs from the STM cooperatively specify the liver fate in the foregut endoderm. (E) As hepatoblasts proliferate and migrate into the STM, the liver diverticulum becomes thicker to form the liver bud. HGF that is expressed in the STM, hepatoblasts, and endothelial cells surrounding the liver bud plays a critical role in the outgrowth of the liver bud. (F) OSM, in a paracrine manner, induces the differentiation of immature hepatocytes to functional hepatocytes of the neonatal liver. HGF is also implicated in hepatocyte differentiation.

3.1. Development of the Liver

Liver development initiates from the endoderm. During late postimplantation, the epiblast gives rise to three germ layers — ectoderm, mesoderm, and endoderm. Nodal, a member of the TGFβ superfamily, is essential for formation of the mesoderm and endoderm during gastrulation in mice and humans [24]. High levels of Nodal signaling specify definitive endoderm and lower levels of Nodal signaling specify mesoderm [25, 26]. Subsequently, transcription factors forkhead box A

(FOXA)2/hepatocyte neculear factor (HNF)3β and GATA binding protein (GATA)4, which are expressed in definitive endoderm, regulate morphogenesis of the foregut [27,28].

Part of the foregut generates the liver bud, the primordial diverticulum that gives rise to the liver parenchyma. Fibroblast growth factors (FGFs) from the cardiac mesoderm and bone morphogenic proteins (BMPs) from the septum transversum mesenchyme (STM) cooperatively specify the liver fate in the foregut endoderm [29,30]. Subsequently, the foregut endoderm forms the liver diverticulum, in which multipotent endoderm cells are committed to liver progenitor cells called hepatoblasts [31]. Hepatoblasts have the capacity to differentiate into hepatocytes that compose the liver parenchyma and the cholangiocyte lining the bile ducts. As hepatoblasts proliferate and migrate into the STM, the liver diverticulum becomes thicker to form the liver bud [32]. Hepatocyte growth factor (HGF) that is expressed in STM, hepatoblasts, and endothelial cells surrounding the liver bud plays a critical role in the outgrowth of the liver bud [33, 34].

Oncostatin M (OSM), in combination with a glucocorticoid such as dexamethasone (DEX), directs hepatoblasts to differentiate into hepatocytes, and then induces hepatic maturation [35]. OSM, an interleukin-6 family cytokine, is a paracrine factor produced by hematopoietic cells.

In contrast to the adult liver, the fetal liver lacks metabolic functions. Instead, it supports the hematopoietic function, which afterward shifts to the bone marrow and the spleen. Like OSM, HGF in the presence of DEX also induces hepatic differentiation and maturation [36]. The fetal liver acquires various additional metabolic functions near birth, and full functions after birth.

3.2. Strategy for Commitment of ES Cells into Hepatocytes

In the last decade, *in vitro* differentiation of ES cells to hepatocytes has been explored by mimicking the liver development process. Most protocols consist of these three steps: directing undifferentiated ES cells into the definitive endoderm (step 1), differentiation of the endodermal cells into liver progenitor cells (step 2), and specification of the liver progenitors to hepatocytes and subsequent maturation (step 3). Here, we overview the representative protocols for induction of hepatocytes from ES cells. Details are summarized in Table 1.

In the first step, undifferentiated ES cells are initially induced to the definitive endoderm. Mainly in classical protocols, embryoid bodies (EBs), which mimic the developing embryo, were formed to induce spontaneous differentiation of ES cells [37-44]. Formed EBs were plated onto plastic dishes coated with an extracellular matrix such as collagen or gelatin. Then, the differentiation process proceeded to the subsequent step, or the cells underwent further endodermal induction by the addition of exogenous factors. While EB formation is useful for inducing an efficient differentiation of ES cells, the resultant cells show a mixed population of three germ layers. Thus, in other protocols, ES cells have been cultured as a monolayer in the presence of exogenous inducers for direct differentiation into the endoderm [45-48]. High concentrations of activin A, a TGFβ family member that binds the same receptors as endogenous endoderm inducer Nodal, have been used [49,50]. Generated endodermal cells have been generally characterized by the expression of FOXA2, SOX17, and GATA4.

In the second step, induced endodermal cells undergo subsequent treatment for specification to hepatic progenitor cells. FGF1, FGF2 and FGF4, and BMP2 and BMP4, which are respectively secreted from the cardiac mesoderm and the STM *in vivo*, have been added for hepatic specification *in vitro* [37, 38, 43-46]. In addition, HGF, which is expressed in the STM and the liver nonparenchymal cells, has been used [37,38,42,44-47].

In this step, hepatic progenitor cells have been characterized mainly by the expression of alpha-fetoprotein (AFP), which is an early fetal hepatic marker, and its expression decreases as the liver develops [51].

Finally, in the third step, hepatic progenitor cells are specified to hepatocytes, and undergo a maturation process. To induce proliferation and differentiation, HGF has been used [37,38,42,43-47]. OSM has also been used for hepatocyte differentiation and further maturation to derive the functions of hepatocytes [37,38,45-48].

Table 1. Protocols for commitment of ES cells into hepatocytes

Species	Differentiation protocol	Hepatic markers/functions	Reference
Mouse	EB formation / FGF1 / HGF / OSM + DEX + ITS	ALB, G6P, TAT, TTR, AAT	[37]
Mouse	EB formation / FGF1 + FGF2 / HGF / OSM + DEX + ITS	ALB, AFP, TAT, Urea synthesis	[38]
Mouse	EB formation / plated onto petridish	AFP, ALB, HNF4α, Transfferin	[39]
Mouse	EB formation / plated onto gelatin-coated plate	AFP, ALB, TTR, AAT, TDO2, CPS1, PEPCK, LST1, FOXA2, ICG uptake	[40]
Mouse	EB formation / plated onto tissue culture plate	AFP, ALB, TTR, AAT, G6P, GST, FOXA1/2/3	[41]
Mouse	EB formation / plated onto gelatin-coated plate, RA + HGF + NGFβ	ALB, G6P, TTR, HNF4α, AAT	[42]
Mouse	EB formation, ActA / FACS sorting, BMP4 + FGF2 + Activin A	FOXA2, ALB, AFP, TAT, CPS1, CYP7A1, CYP3A11, ALB production, PAS staining	[43]
Mouse	EB formation / ActA + FGF2 / co-cultured with human nonparenchymal liver cell lines, dHGF + DMSO / DEX	ALB, CK18, TAT, G6P, FOXA2, HNF4α, CYP7A1, CK19, AFP, ammonia detoxification, glucose production, metabolism of lidocaine and diazepam	[44]
Mouse	Monolayer on gelatin-coated plate, RA / passaged onto collagen-coated plate, HGF + FGF1 + FGF4 / OSM + DEX	ALB, TTR, TAT, G6P, TDO2, CK8, LST1, CPS1, PEPCK, CYP1A1, FOXA2, HNF4α, CK18, ALB, fibrinogen synthesis	[45]
Human	Monolayer / ActA / ActA + ITS / FGF4 + BMP2 / HGF /OSM + DEX	AFP, ALB, CK8, CK18, G6P, AAT, HNF4α, PEPCK, TDO2, TAT, CYP7A1, CYP3A4, CYP2B6, LDL uptake, ICG uptake, PAS staining, PROD	[46]
Human	Monolayer / DMSO / HCM + HGF + EGF / HCM + HGF + OSM	AFP, ALB, AAT, TDO2, HNF4α, C/EBPα, TTR, Hepar 1, CYP3A4 activity, PAS staining, ICG uptake and excretion	[47]
Human	Monolayer on matrigel-coated plate, SB + ActA / passaged onto matrigel-coated plate, DMSO / HGF + OSM	AFP, ALB, TAT, TDO2, TTR, CAR, ApoF, Pax6, c-Met, CK18, CK19, CYP2C9, CYP2C19, CYP2D6, CYP3A4, CYP3A7, PAS staining, CYP3A4 enzyme activity, fibrinoven, fibronectin, and α-2 macroglobulin production	[48]

AAT, α1-antitrypsin; ActA, activin A; ApoF, apolipoprotein F; CPS-1, carbamyl phosphate synthetase 1; EGF, epidermal growth factor; dHGF, HGF with deletion of 5 amino acids; GST, glutathione-S-transferase; ICC, immunocytochemistry; ITS, insulin-transferrin-selenium; LST1, liver specific organic anion transporter-1; PAS, periodic acid-Schiff; PEPCK, phosphoenolpyruvate carboxykinase; PROD, entoxyresorufin-O-dealkylas; RA, retinoic acid; SB, sodium butyrate; TTR, transthyretin.

In addition, dexamethasone, a synthetic glucocorticoid, has been used to induce the enzyme activity of hepatocytes such as glucose-6-phosphatase (G6P), tyrosine aminotransferase (TAT), and cytochrome P450 (CYP)s [37,38,44-46]. Mature hepatocytes have been characterized mainly by the expression of albumin (ALB), tryptophan 2,3-dioxygenase (TDO2) and TAT.

4. Generation of Hepatocytes from iPS Cells

4.1. Current Status of Research on Hepatic Differentiation of iPS Cells

Recently, researchers have confirmed that iPS cells can be differentiated into authentic hepatocytes

by *in vivo* experiments. Si-Tayeb *et al.*, by examining embryos derived solely from mouse iPS cells by tetraploid complementation, first confirmed that iPS cells were competent to follow a hepatic developmental program that produced all liver cell lineages [53]. Espejel *et al.*, by generating chimeric mice in which all hepatocytes were iPS cell-derived, also confirmed that iPS cell–derived hepatocytes have the functional and proliferative capabilities needed for liver regeneration in mice [59]. Moreover, they demonstrated that fibroblast origin and reprogramming did not diminish the regenerative capabilities of iPS cell–derived hepatocytes by challenging 2/3 partial hepatectomy or transplantation into liver-diseased mice.

Table 2. Protocols for commitment of iPS cells into hepatocytes

Species/origin	Differentiation protocol	CYP expression	Reference
Human / fibroblast	Adherent culture on MEF feeder cells, ActA / FGF4 + BMP2 / HGF + KGF / OSM + DEX / OSM + DEX + N2 + B27	2A6 (mRNA), 2B4 (enzyme activity), 3A4 (mRNA, ICC)	[52]
Human / foreskin fibroblast	Monolayer on matrigel-coated plate, ActA B27 / B27 + BMP4 + FGF2 / B27 + HGF, 4%-O_2 / OSM	Not detected.	[53]
Human / fibroblast	Monolayer on matrigel, ActA + Wnt3a / Act / DMSO / HGF + OSM	1A2, 3A4 (enzyme activitiy), 7A1 (mRNA)	[54]
Mouse / MEF	Monolayer on gelatin-coated plate, DMSO / SB	7A1 (mRNA)	[55]
Mouse / fibroblast	EB formation / plated onto matrigel-coated plate, ActA + Wnt3 / FGF2 + DMSO / HGF + DMSO / HGF + OSM + DEX	1A1 (ICC)	[56]
Human / hepatocyte	Monolayer, ActA / passaged onto collagen I-coated plate, FGF4 + HGF / FGF4 + HGF + OSM + DEX	1A2 (enzyme activity), 3A4 (ICC, enzyme activity)	[57]
Human / fibroblast	Monolayer, ActA + FGF2 + BMP4 / FGF10 / FGF10 + RA + SB431542 / FGF4 + HGF + EGF	Not determined.	[58]
Mouse / MEF	Generation of chimeric mice by injection of iPS cells into blastocysts obtained from FAH-deficient mice	Not determined.	[59]
Human / dermal fibrobalst	Monolayer, ActA + BMP4 / ActA + FGF2 + B27 / ActA / HGF + OSM	3A4 (enzyme activitiy)	[60]
Human / foreskin fibroblast	Co-cultured with human ES cell-deirved fibroblast like cells	7A1 (mRNA), ethoxyresorufin-O-deethylase activity	[61]
Human / skin fibroblast	EB formation / plated onto matrigel-coated plate, ActA / DMSO + HGF/ DEX	1A1 (ICC), 3A4 (mRNA), pentoxyresorufin O-dealkylase activity	[62]
Human / embryonic lung fibroblast	Monolayer on laminin-coated plate, ActA + FGF2 / BMP4 + FGF4 / adenoviral transduction of HEX, BMP4 + FGF4 / FGF4 + HGF + OSM + DEX	2D6, 7A1 (mRNA), 3A4 (mRNA, enzyme activity)	[63]
Mouse / MEF	EB formation / plated onto gelatin-coated plate, ActA + FGF2 / HGF	Not determined.	[64]
Mouse / bone marrow adherent cell	Monolayer on matrigel-coated plate, ActA + Wnt3a / BMP4 + FGF2 /FGF1 + FGF4 + FGF8 / HGF + Follistatin	3A7, 7A1 (mRNA), 1A2 (enzyme activity)	[65]
Human / fetal foreskin fibroblast	Monolayer, ActA + SB / DMSO / HGF + OSM	1A1, 2C9, 2E1, 2F1, 2C19, 11B2 (mRNA)	[66]

FAH, fumarylacetoacetate hydrolase; ICC, immunocytochemistry; KGF, keratinocyte growth factor; MEF, mouse embryonic fibroblast; N2, N2 supplement; B27, B27 supplement.

Meanwhile, an increasing number of reports have demonstrated that iPS cells can be directed into hepatocytes *in vitro*. Most of them have followed protocols that were established based on the knowledge regarding *in vitro* differentiation of ES cells to hepatocytes (Table 2). The majority of the protocols described involve a direct induction to differentiate into endoderm, hepatic progenitors, and

mature hepatocytes using a stepwise differentiation method. Of these, Inamura *et al.* proposed a challenging method to generate hepatoblasts from human iPS cells by adenovirus-mediated overexpression of the HEX gene, a homeotic gene essential for hepatic differentiation [63]. Others include an initial step of EB formation and co-culture with supporting cells.

Differentiated hepatocytes have been characterized by the expression of a panel of marker genes at the mRNA level and/or protein level. Their functionality has been confirmed by albumin secretion, urea secretion, glycogen storage, low-density lipoprotein (LDL) uptake, indocyanine green (ICG) uptake and release, and CYP activity.

A more stringent test of the differentiation ability would be an *in vivo* functionality of the differentiated cells. Accordingly, Si-Tayeb *et al.* and Gai *et al.* demonstrated that iPS cell-derived hepatocytes had the inherent capacity to integrate into the hepatic parenchyma *in vivo* [53,56].

Applying stem cell technology to cell replacement therapy in liver diseases has long been desired, though it has not yet been realized.

As alternatives to orthotopic liver transplantation, cell replacement therapy in the form of hepatocyte transplantation and artificial livers including extracorporeal and intracorporeal devices have been explored [2,67,68]. However, these approaches require a much larger amount of hepatocytes than currently available [68]. Therefore, researchers have aimed at obtaining transplantable cells from other sources such as ES cells, adult stem cells, or liver progenitor cells.

Of these, ES cells have attracted the most attention since they provide an unlimited cell source owing to their infinite proliferative capacity. However, the clinical application of ES cells involves immune rejection after transplantation and ethical concerns regarding the use of human embryos.

4.2. Possibility of iPS Cells as a Cell Source for Cell Replacement Therapy

iPS cells may be able to completely overcome the obstacles associated with human ES cells, thus the technology to generate hepatocytes from iPS cells has created enthusiasm for their potential applications in cell replacement therapy.

In cases where a sporadic form of a disease is due to epigenetic alterations in the liver, iPS cells derived from somatic cells from non-hepatic tissues could be therapeutic, since the reprogramming process should reverse the disease causing the epigenetic modifications. In contrast, in cases where specific genotypes are the root cause of diseases (for example, Crigler-Najjar syndrome, Wilson's disease and tyrosinemia), reprogramming will not alleviate the problem.

In such cases, the resultant iPS cell-derived hepatocytes may succumb to the same degenerative processes that occurred in the patient. If a genetic defect is known, utilizing gene therapy approaches could restore cellular function. Several reports have provided proof-of-concept that iPS cell technology can be used for the generation of disease-corrected, patient-specific cells [69-71].

Hanna *et al.* corrected the mutant gene of iPS cells derived from an anemic mouse, differentiated them into hematopoietic progenitors, and importantly, demonstrated that these cells ameliorated some pathological features after transplantation back into the mouse [69].

Another attempt to apply iPS cells to cell replacement therapy is the generation of organs derived from donor iPS cells, using a xenogenic environment. Kobayashi *et al.* generated interspecific chimeras by injecting mouse or rat iPS cells into rat or mouse blastocysts, respectively, and confirmed that iPS cells were able to contribute to xenogenic development between mouse and rat [72].

Notably, they found that rat wild-type iPS cells injected into Pdx-/- (pancreatogenesis-disabled) mouse blastocysts generated a normally functioning rat pancreas in Pdx1-/- mice. This finding allows us to expect that a blastocyst complementation of hepatogenesis-disabled large animals such as pigs with human iPS cells should be able to generate a whole functioning human liver.

Despite the large concern about safety at this moment, the realization of such a strategy has the possibility to solve the current donor shortage problem in liver transplantation.